Controls of Dynamic and Static Stress Changes and Aseismic Slip on Delayed Earthquake Triggering: Application to the 2019 Ridgecrest Earthquake Sequence

Jeena Yun[1], Alice-Agnes Gabriel[1,2], Dave A. May[1], and Yuri Fialko[1]

[1]Scripps Institution of Oceanography, University of California San Diego, La Jolla, CA, USA
[2]Department of Earth and Environmental Sciences, Ludwig-Maximilians Universität München, Munich, Germany

Key Points:

- Simulations of stress perturbations due to the M_w 5.4 foreshock predict a clock advance of the mainshock of several hours.
- Instantaneous triggering does not occur unless stress perturbation is a large fraction of strength excess during quasi-static nucleation.
- The sign of stress perturbation in areas of accelerating slip controls the advance versus delay of the mainshock.

Corresponding author: Jeena Yun, j4yun@ucsd.edu

Abstract

Dynamic earthquake triggering often involves a time delay relative to the peak stress perturbation. In this study, we investigate the physical mechanisms responsible for delayed triggering. We compute detailed spatiotemporal changes in dynamic and static Coulomb stresses at the 2019 M_w 7.1 Ridgecrest mainshock hypocenter, induced by the M_w 5.4 foreshock, using 3D dynamic rupture models. The computed stress changes are used to perturb simulations of 2D quasi-dynamic sequences of earthquakes and aseismic slip on the mainshock fault governed by rate-and-state friction. We explore multiple scenarios with varying hypocenter depths, perturbation amplitudes and timing, and different evolution laws (aging, slip, and stress-dependent). Most of the perturbed models show a mainshock clock advance of several hours. Instantaneous triggering occurs only if the peak stress perturbation is comparable to the strength excess during quasi-static nucleation. While both aging and slip laws yield similar clock advances, the stress-dependent aging law results in a systematically smaller clock advance. The sign of the stress perturbation in regions of accelerating slip controls whether the mainshock is advanced or delayed. Mainshocks can be triggered even when the future mainshock hypocenter is within a stress shadow, due to stress transfer from the foreshock sequence. Our results imply that the Ridgecrest mainshock fault was already on the verge of runaway rupture prior to the M_w 5.4 foreshock. These results highlight the contribution of both foreshocks and aseismic deformation to earthquake triggering and emphasize the importance of considering the physics of fault-system-wide processes when assessing triggering potential.

Plain Language Summary

Earthquakes can be triggered by stress changes induced by seismic waves from other earthquakes. These triggered events often exhibit a delay relative to the arrival time of the seismic waves. For example, the 2019 M_w 7.1 Ridgecrest, CA, mainshock occurred several hours after a nearby M_w 5.4 foreshock. The physical mechanism behind such delayed triggering remains unclear. In this study, we use computer simulations to explore the physical mechanisms responsible for delayed triggering. We compute detailed time-dependent stress changes at the Ridgecrest mainshock hypocenter caused by the M_w 5.4 foreshock and compare the timing of the mainshock in models with and without stress perturbation, for different scenarios. These results show that in most cases the perturbed mainshock occurs several hours earlier than it would without the perturbation. The clock advancement or delay depends on whether the stress change in regions of accelerating fault slip favors rupture. Even when stress changes at the future mainshock hypocenter do not favor rupture, stress transfer from the foreshock sequence can still trigger mainshocks. We infer that the Ridgecrest mainshock fault was ready to rupture. These findings emphasize the important role of foreshock sequences and aseismic deformation in earthquake triggering.

1 Introduction

Some earthquakes may be encouraged by other earthquakes, a phenomenon called earthquake triggering (e.g., Freed, 2005; Hill & Prejean, 2015; Stein, 1999). Earthquake triggering has been documented using seismic and geodetic observations at various distances from the source, both in the near-field (within one or two fault lengths; e.g., Bosl & Nur, 2002; Hudnut et al., 1989; King et al., 1994; Parsons & Dreger, 2000) and far-field (e.g., DeSalvio & Fan, 2023; Gomberg et al., 2001; Hill et al., 1993). Earthquake triggering has also been observed in laboratory experiments (e.g., Dong et al., 2022; Farain & Bonn, 2024; Y. Jin et al., 2021). One of the widely used frameworks to explain earthquake triggering considers changes in Coulomb failure stress (ΔCFS; Caskey & Wesnousky, 1997; Harris & Simpson, 1992; King et al., 1994; Z. Jin et al., 2022). Slip on a fault can permanently alter the stress field, either promoting or inhibiting failure on surrounding

faults. The static ΔCFS is a linear combination of permanent changes in shear stress and effective normal stress on a given 'receiver' fault. The magnitude and sign of ΔCFS indicate whether a fault is moved closer to failure. A region with positive static ΔCFS is considered to have an elevated likelihood of failure and is often well correlated with an increased rate of aftershocks, although there are notable exceptions (e.g., Hardebeck & Harris, 2022).

However, not all earthquakes appear to be triggered by static ΔCFS. Some presumably triggered earthquakes occur in regions with negative ΔCFS (stress shadow; Felzer & Brodsky, 2005) and at considerable distances from the causative earthquakes (e.g., Gomberg, 1996). The magnitude of static stress changes decreases rapidly with distance, becoming negligible at teleseismic distances (Árnadóttir et al., 2004; Gomberg et al., 2001). The concept of dynamic triggering considers changes in stress and/or strength due to passing seismic waves, which can produce an order of magnitude higher ΔCFS compared to static stress changes (Felzer & Brodsky, 2006; Kilb et al., 2000). Dynamic triggering may possibly explain the asymmetry in aftershock distributions due to rupture directivity (Kilb et al., 2000) and the occurrence of aftershocks within static stress shadows (Hardebeck & Harris, 2022). Additionally, dynamically triggered earthquakes often occur in geothermal fields or volcanic regions (e.g., Brodsky & Prejean, 2005), suggesting an important role of pore fluids interacting with faults.

While some dynamically triggered earthquakes occur at the time of the largest stress perturbation during the passage of seismic waves, a time delay between the largest perturbation and triggered earthquakes is frequently observed (e.g., Belardinelli et al., 1999; Dong et al., 2022; Guo et al., 2024; Shelly et al., 2011). For example, the July 2019 M_w 7.1 Ridgecrest, California, earthquake was preceded by multiple foreshocks, including the two largest events of M_w 6.4 and M_w 5.4 (Jia et al., 2020; Meng & Fan, 2021; Ross et al., 2019). Previous studies suggest that the nucleation site of the M_w 7.1 Ridgecrest mainshock likely experienced significant dynamic stress changes, on the order of several MPa, due to foreshocks (e.g., Barnhart et al., 2019; Z. Jin & Fialko, 2020; Taufiqurrahman et al., 2023). Another example is the February 2023 Kahramanmaraş, Turkey, M_w 7.8-7.7 earthquake doublet, which exhibited a time difference of about 9 hours between the two earthquakes. The M_w 7.8 earthquake induced a large dynamic stress perturbation on the M_w 7.7 earthquake fault plane (Gabriel et al., 2023; Jia et al., 2023). Given the spatiotemporal proximity of the causative and triggered large earthquakes, it is important to understand why apparently large stress perturbations fail to instantaneously trigger faults that are presumably already on the verge of runaway rupture, and what factors control delayed triggering.

Several hypotheses have been proposed to explain the observed time delay in dynamic earthquake triggering, including changes in frictional contacts (Parsons, 2005), aseismic slip triggered by dynamic (Árnadóttir et al., 2004; Shelly et al., 2011) or static (Barbot et al., 2009; Wang & Fialko, 2014) stress changes, variations in pore pressure or fluid diffusion (Elkhoury et al., 2006; Gomberg et al., 2001), granular flow (Farain & Bonn, 2024; Johnson & Jia, 2005), and subcritical crack growth (Atkinson, 1984). Recently, Dong et al. (2022) observed delayed dynamic triggering in laboratory experiments. They infer a slow rupture phase and an increased critical slip distance near the P-wave perturbation, indicating a contribution of aseismic slip and changes in frictional contacts to delayed dynamic triggering.

Insights into the mechanics of earthquake triggering can be obtained from numerical modeling. Rate-and-state friction is a widely adopted constitutive law that describes the non-linear response of rock friction as a function of slip velocity and the state of the interface (Dieterich, 1979; Ruina, 1983). Single-degree-of-freedom spring slider models have provided useful insights into time-dependent slip histories and the sensitivity of the nucleation time in response to static or dynamic stress perturbations (Dieterich, 1994; Gomberg et al., 1997; Perfettini et al., 2001; Mitchell et al., 2015). More complex rate-

and-state models incorporating sequences of earthquakes and aseismic slip (SEAS) have enhanced the understanding of the effects of external stress perturbations on the temporal evolution of fast and slow slip instabilities (e.g., Kostka & Gallovič, 2016; D. Li & Gabriel, 2024; Perfettini et al., 2003a, 2003b; Tymofyeyeva et al., 2019; Wei et al., 2018).

Despite considerable progress, many aspects of the physical mechanisms underlying earthquake triggering and delay remain unresolved. While far-field triggering is most likely dynamic in nature, distinguishing between the effects of static and dynamic triggering in the near-field is challenging. In the near-field, van der Elst and Brodsky (2010) estimated that dynamic strain accounts for the occurrence of 15 % - 60 % of magnitude 3 - 5.5 earthquakes, and Hardebeck and Harris (2022) estimated that ∼34 % of all aftershocks are driven by dynamic stress changes. However, these studies relied on order-of-magnitude estimates of dynamic strain to quantify the effects of dynamic triggering. Although some previous studies have explored the effects of static (Dublanchet et al., 2013; Kaneko & Lapusta, 2008; Perfettini et al., 2003a) and dynamic (Gomberg et al., 1997; Perfettini et al., 2001, 2003b) stress changes individually, the combined static and dynamic effects remain poorly understood.

Also, existing models of dynamic triggering typically rely on simplified stress histories to estimate the triggering response. For example, dynamic stress perturbations are often modeled as a single pulse or harmonic function (Ader et al., 2014; Perfettini et al., 2003b; Luo & Liu, 2019). A notable exception is Wei et al. (2018), who computed a detailed time series of ΔCFS inferred from a kinematic slip model, but neglected variations of ΔCFS with depth. While these simplified stress histories might be appropriate approximations for far-field triggering or near-surface processes, they fall short of capturing the complexities of near-field triggering mechanics. A comprehensive understanding of near-field triggering requires considering the detailed history of stress perturbation throughout the full seismogenic depth range.

The emergence of earthquake dynamic rupture and SEAS simulations that efficiently utilize high-performance computing (HPC) provides new opportunities to address existing knowledge gaps (e.g., Taufiqurrahman et al., 2023; Uphoff et al., 2023). High-accuracy 3D dynamic rupture simulations enable the computation of realistic histories of seismic stress perturbations, allowing the exploration of the combined contributions of static and dynamic stress changes. Similarly, HPC-empowered SEAS simulations can incorporate more realistic parameters that are closer to those observed in laboratory experiments and allow extensive exploration of the parameter space. Additionally, the increased computational capabilities facilitate volume-discretized methods (Erickson & Dunham, 2014; Liu et al., 2020; Pranger, 2020; Thakur et al., 2020; Uphoff et al., 2023), which can require high computational costs in terms of both storage and time-to-solution.

In this study, we investigate the physical factors and processes underlying earthquake triggering, using the 2019 M_w 7.1 Ridgecrest earthquake sequence as a case study. The M_w 7.1 Ridgecrest mainshock initiated on a primarily right-lateral northwest-striking fault, rupturing multiple conjugate faults (Ross et al., 2019). The M_w 6.4 foreshock occurred about 34 hours before the mainshock, rupturing both a northeast-striking left-lateral fault and a northwest-striking right-lateral fault (Magen et al., 2020; Jia et al., 2020; S. Li et al., 2020). The M_w 5.4 foreshock occurred on a left-lateral southwest-striking fault (Shelly, 2020), 16.2 hours prior to the mainshock. Its hypocenter is located $\sim$ 3 km away from the M_w 7.1 mainshock (USGS, 2020), making it the closest M5+ event in both space and time to the mainshock hypocenter (Fig. 1). Kinematic and dynamic rupture models suggest that the M_w 6.4 foreshock increased ΔCFS near the Ridgecrest mainshock hypocenter, likely bringing the mainshock fault closer to failure (e.g., Goldberg et al., 2020; Taufiqurrahman et al., 2023; Wang et al., 2020). Seismicity migration patterns imply that the M_w 5.4 foreshock played a crucial role in triggering the mainshock (Huang et al., 2020; Yue et al., 2021). Barnhart et al. (2019) inferred a considerable increase in static ΔCFS due to the M_w 5.4 foreshock, and Z. Jin and Fialko (2020) esti-

mated dynamic ΔCFS perturbations of orders of megapascals on the mainshock fault plane. Laboratory experiments suggest that frictional interfaces are highly sensitive to stress perturbations during the nucleation of unstable slip (e.g., van der Elst & Savage, 2015). This raises the question of why the M_w 5.4 foreshock, despite producing large stress changes in close spatial and temporal proximity to the mainshock, did not instantaneously trigger runaway rupture (Barnhart et al., 2019; Huang et al., 2020; Z. Jin & Fialko, 2020). Here, we focus specifically on the potential triggering relationship between the M_w 5.4 foreshock and the M_w 7.1 mainshock. These two events provide insight into delayed triggering on a fault that was likely already in the nucleation phase of a major earthquake, due to prior stressing history, including interseismic loading and nearby events such as the M_w 6.4 foreshock.

We record detailed spatiotemporal stress changes on the mainshock fault plane caused by the M_w 5.4 foreshock, considering a range of fault geometries and varying moment release rates using 3D dynamic rupture simulations (Sections 2.1 and 3.1). These stress perturbations are applied to a suite of quasi-dynamic SEAS simulations described in a companion paper (Yun et al., 2025a), denoted YGMF1 hereafter. The unperturbed models represent the reference fault slip history on the mainshock fault. We extensively explore the change in timing of the mainshock (i.e., mainshock 'clock change') across different stress perturbation models, target mainshock depths, times intervals between perturbation and mainshock, amplitudes of stress perturbations, and state variable evolution laws (Sections 3.2 and 3.3). We compare the correlation of the mainshock clock change with various physical factors, such as peak slip rate, static ΔCFS, and peak dynamic ΔCFS, to identify the controlling mechanisms behind the mainshock clock change. We find that the spatial distribution of depth-dependent static ΔCFS and aseismic deformation significantly affects the mainshock clock change (Section 4.3). This can be well captured by our newly proposed metric, W (Eq. (7)). Our study proposes a novel framework for evaluating the combined effect of static and dynamic stress changes on near-field triggering and suggests a deterministic approach to estimating triggering potential. Additionally, we highlight the contributions of static stress change and background deformation in earthquake triggering and advocate for an integrative approach to assessing triggering potential.

2 Methods

2.1 Dynamic Rupture Simulations

We compute the coseismic spatiotemporal evolution of stress changes near the mainshock hypocenter location caused by the M_w 5.4 foreshock using 3D dynamic rupture simulations. To this end, we use the open-source dynamic rupture and seismic wave propagation simulation software *SeisSol* (Dumbser & Käser, 2006; Pelties et al., 2014), which is optimized for HPC infrastructure (Heinecke et al., 2014; Krenz et al., 2021; Uphoff et al., 2017) and has been applied to model rupture dynamics in various tectonic contexts (e.g., Biemiller et al., 2022; Ulrich et al., 2019). We include both foreshock and mainshock faults within a 3D domain (Fig. 2a). In this model setup, the mainshock fault plane serves as the receiver plane, recording the dynamic and static stresses induced by the foreshock.

The foreshock rupture plane is modeled as a square fault with dimensions of 3 km by 3 km, centered at a depth of 7 km (USGS, 2017). We retrieve the focal mechanism of the M_w 5.4 foreshock from USGS ComCat (USGS, 2017). Among the two nodal planes, we choose the southwest-striking plane as the fault plane, following Shelly (2020). We consider two dip angles, vertical and NW70° dip (USGS, 2017), to account for possible uncertainties in the fault dip estimation. To nucleate the earthquake, we prescribe a frictionally weak circular patch with a radius of 250 m at the center of the foreshock rupture plane.

The receiver mainshock fault extends from the free surface to a depth of 24 km, with a width of 3 km, and is centered at the M_w 7.1 mainshock epicenter location (USGS, 2017). We model scenarios using four different mainshock fault strikes (320°, 330°, 340°, and 350°) to cover a range of the average strike angles obtained from finite fault inversions of the M_w 7.1 mainshock (320°; Z. Jin & Fialko, 2020; Jia et al., 2020) and focal mechanisms (340°; SCEDC, 2013; Z. Jin & Fialko, 2020). Allowing for variations in the strike and dip of either fault accounts for uncertainties in the relative geometries of the two faults. Since we use eight different combinations of mainshock fault strikes and foreshock fault dips, the minimum distance between the two faults varies between 116 m and 1303 m. For models with a dipping foreshock fault, the horizontal extent of the mainshock fault is slightly reduced by 20 m (330°) or 500 m (320°) to prevent the two faults from intersecting. However, this variability in horizontal extent does not affect the stress change estimates, as we focus on the stress changes along a profile beneath the mainshock epicenter. We confirm that nearly identical stress change estimates are produced when placing multiple point receivers along the same profile.

We embed both faults in a 3D velocity model (CVMS4.26.M01; Lee et al., 2014; Small et al., 2017, 2022). We use a stress-free boundary condition for the flat free surface (at zero depth) and absorbing boundary conditions for all remaining model boundaries. The spatial discretization of dynamic rupture simulations must be sufficient to resolve the width of the process zone (Day et al., 2005; Ramos et al., 2022). We use a uniform element size of 25 m on the foreshock fault. This discretization adequately resolves the median cohesive zone width of about 200 m on the foreshock fault (Wollherr et al., 2018). For the mainshock fault, we use an element size of 80 m. This model resolves the seismic wavefield up to frequencies of 6.9 Hz between the two faults. Away from the fault, we gradually coarsen the unstructured tetrahedral mesh to element sizes of up to 1.5 km at the boundaries of our computational domain. The meshes used in this study contain 1.8 to 2.3 million elements and require ∼500 CPU hours on average on the supercomputer SuperMUC-NG for each 15-second simulation.

All dynamic rupture model parameters used in this study are summarized in Table S1. We use a linear slip-weakening friction law (Andrews, 1976; Ida, 1972; Palmer & Rice, 1973) where the fault strength τ_s is defined as

$$\tau_s = C_0 + \sigma_n \left(f_s - \frac{f_s - f_d}{D_{LSW}} \min(S, D_{LSW}) \right), \tag{1}$$

with the frictional cohesion C_0, the effective normal stress σ_n, the static and dynamic friction f_s and f_d, respectively, and the slip-weakening distance for the linear slip-weakening law D_{LSW}. We vary the combination of dynamic friction f_d and critical distance D_{LSW} to obtain models with different rupture characteristics (Table S1).

We assign a Cartesian initial stress tensor $\boldsymbol{\sigma}$ for the entire domain (Table S1). As a result, the initial normal and shear stresses on each fault vary depending on the fault orientation. For the foreshock fault, which is contained within the $xz-$plane, the initial normal stress is $\sigma_n^0 = \boldsymbol{\sigma}_{yy}$, and the initial shear stress $\tau_0 = \boldsymbol{\sigma}_{xy}$. The prestress level and the frictional fault strength can be characterized by the seismic parameter or relative strength parameter S (Andrews, 1976), which represents the ratio of the frictional strength excess to the maximum possible dynamic stress drop,

$$S = \frac{f_s \sigma_n^0 - \tau_0}{\tau_0 - f_d \sigma_n^0}, \tag{2}$$

where $f_s \sigma_n^0$ and $f_d \sigma_n^0$ are the static and dynamic strength, respectively. Smaller static and dynamic friction coefficients are assigned within the nucleation patch, resulting in an S ratio of -0.56, which gradually increases outside the patch towards the fault boundary (Fig. 2b).

From the stress changes recorded on the mainshock fault plane, we compute the time evolution of ΔCFS, which includes both static and dynamic stress changes, as follows:

$$\Delta\mathrm{CFS}(z,t) = \hat{\tau}(z,t) - f\hat{\sigma}_n(z,t) \tag{3}$$

where z is depth, $t \in [0\text{ s},\ 15\text{ s}]$ is time, $f = 0.4$ is the friction coefficient, and $\hat{\sigma}_n$ and $\hat{\tau}$ are the normal and along-strike shear stress changes with respect to the initial conditions. The peak dynamic ΔCFS at a certain depth then becomes $\max_t \Delta\mathrm{CFS}(z,t)$, and the static ΔCFS at a certain depth is $\Delta\mathrm{CFS}\ (z, 15\text{ s})$. Since models with varying dip angles and moment rate functions yield slightly different total moments, we scale all stress estimates by a factor of $M_{5.4}/M_0$ where $M_{5.4}$ is the total moment expected for a magnitude 5.4 earthquake on the modeled foreshock fault, and M_0 is the total moment obtained from each model.

2.2 Reference SEAS Simulations

A companion paper YGMF1 explores the role of various heterogeneities on the slip complexity in 2D antiplane quasi-dynamic SEAS simulations on a vertical strike-slip fault governed by the rate-and-state friction law, using the open-source software *Tandem* (Uphoff et al., 2023). These simulations assume a 1D planar fault embedded in a 2D elastic half-space (Fig. S1). YGMF1 also compares slip patterns obtained from two state evolution laws, the aging law (Dieterich, 1979):

$$\frac{d\theta}{dt} = 1 - \frac{\|\boldsymbol{V}\|\theta}{D_{RS}}, \tag{4}$$

and the slip law (Ruina, 1983):

$$\frac{d\theta}{dt} = -\frac{\|\boldsymbol{V}\|\theta}{D_{RS}} \ln\left(\frac{\|\boldsymbol{V}\|\theta}{D_{RS}}\right), \tag{5}$$

where $\|\boldsymbol{V}\|$ is the Euclidean norm of the slip rate vector $\boldsymbol{V}$, θ is the state variable, and D_{RS} is the characteristic state evolution distance.

In this study, we use the most complex model considered in YGMF1 (model N12R4D4; see their Section 3.2) as the reference model of slip history on the 2019 Ridgecrest mainshock fault without stress perturbation. This model features cascades of ruptures with various sizes and hypocenter depths as well as spontaneous slow slip events (SSE), as shown in Figure S2a. In particular, the model exhibits temporal clustering of small earthquakes preceding a larger earthquake (Fig. S3), resembling foreshock-mainshock sequences observed on natural faults (e.g., Helmstetter et al., 2003; Jones & Molnar, 1979; Reasenberg, 1999). We denote this model A2 (where 'A' stands for aging law and '2' stands for the average D_{RS} of 2 mm). In this model, mainshock hypocenters commonly occur between ∼3-8 km depth, reflecting the imposed spatial distribution of rate-and-state parameters, particularly transitions between creeping (velocity-strengthening) and locked (velocity-weakening) fault regions (Fig. S1). These rheological transitions, inherited from model A2 in our companion study (YGMF1), localize stress accumulation at multiple depths. While this depth range may appear shallow for $M > 7$ events, it is consistent with published estimates of the 2019 M_w 7.1 Ridgecrest mainshock, which vary between ∼2-8 km depending on the analysis method (Hauksson & Jones, 2020; Z. Jin & Fialko, 2020). We also use models N12R4D6-S that assumes slip law (Fig. S2b) and N12R4D6 that assumes aging law (Fig. S2c) from YGMF1 (see their Section 3.4) to compare the triggering response of different evolution laws. We denote these models S10 (where 'S' stands for slip law and '10' stands for the average D_{RS} of 10 mm) and A10, respectively. All SEAS model input parameters used in this study are summarized in Table S2.

We consider an additional state evolution law that can capture the immediate response of the rock strength as a response to a sudden change in normal stress (e.g., Boettcher

& Marone, 2004; Linker & Dieterich, 1992; Pignalberi et al., 2024). The effect of external normal stress perturbations is taken into account by adding a stress-dependent term to the classic state evolution laws. For example, the stress-dependent aging law takes the form of:

$$\frac{d\theta}{dt} = 1 - \frac{\|\boldsymbol{V}\|\theta}{D_{RS}} - \alpha\frac{\theta}{b}\frac{\dot{\sigma}_n}{\sigma_n}, \tag{6}$$

where b is the rate-and-state parameters governing the evolution effect, $\dot{\sigma}_n$ is the time derivative of normal stress, and α is the scaling factor that can vary from 0 to the static friction coefficient (Boettcher & Marone, 2004; Wei et al., 2018). We use $\alpha = 0.3$ (Boettcher & Marone, 2004; Richardson & Marone, 1999). The stress-dependent aging law takes effect only under external stress perturbations, as normal stress remains constant in 2D antiplane models.

Following YGMF1, we define 'system-size earthquake' as an event that ruptures the entire seismogenic zone (rupture length greater than 10 km), while all other events are denoted 'partial rupture events'. We use the term 'mainshock' interchangeably with 'system-size earthquake'. We identify 'foreshocks' as temporally clustered partial ruptures that ultimately lead to a mainshock (i.e., a system-size earthquake). We describe foreshocks as 'cascading' when they are densely spaced. The term 'leading foreshock' denotes the first foreshock (i.e., the first partial rupture) in such a cascading foreshock sequence, e.g., as illustrated by green diamonds in Figure S3. 'Runaway rupture' denotes the stage at which a slip patch that has exceeded the critical nucleation dimensions becomes self-sustaining. The elastodynamic stress concentration at the rupture front supplies enough energy release to overcome friction everywhere ahead of it, so the rupture accelerates and propagates until it meets a large strength/stress barrier or the geometric limit of the fault (Ampuero & Rubin, 2008; Andrews, 1976; Galis et al., 2017; Garagash & Germanovich, 2012; Lapusta et al., 2000; Mosconi et al., 2025).

2.3 Combining Dynamic Rupture and SEAS Simulations

To estimate the triggering response of the mainshock nucleation site to stress changes imposed by the foreshock, we perturb the SEAS models (Section 2.2) using stress histories calculated from the dynamic rupture simulation (Section 2.1). The main processing steps are as follows (Fig. 3):

1. Run 3D dynamic rupture models rupturing the foreshock fault and record the normal ($\hat{\sigma_n}$) and shear stress ($\hat{\tau}$) perturbations across the (locked) mainshock fault beneath the mainshock epicenter (Section 2.1; Fig. 3b).
2. Run a 2D SEAS model and obtain N cycles using either the aging law or the slip law. We refer to these models as 'unperturbed' reference models (black line in Fig. 3a).
3. Among the N cycles of the unperturbed SEAS model, choose one cycle with a system-size earthquake. The selected system-size earthquake will be called a 'target mainshock'. Identify the time of occurrence for the target mainshock, t_u.
4. Restart and run the cycling experiment from time $t = t_u - \Delta t_g$ where Δt_g is the time interval between the start of the perturbation (corresponding to the time of the M_w 5.4 foreshock) and the mainshock. Unless otherwise noted, Δt_g is set to 16.2 h, the time interval between the M_w 5.4 foreshock and the M_w 7.1 mainshock in the 2019 Ridgecrest earthquake sequence (USGS, 2017). During this stage, the time-dependent normal ($\hat{\sigma}_n$) and shear ($\hat{\tau}$) stress changes on the mainshock fault simulated in the dynamic rupture simulations (Section 2.1) are added to those of the unperturbed SEAS model ($\tau(z,t)$ & $\sigma_n(z,t)$) at each time step, yielding the perturbed normal stress (σ_n^p) and shear stress (τ^p):

$$\tau^p(z,t) = \tau(z,t) + \hat{\tau}(z,t)$$

$$\sigma_n^p(z,t) = \sigma_n(z,t) + \hat{\sigma}_n(z,t).$$

This phase will be denoted as the 'perturbation period', which lasts 15 s. During this stage, we use a fixed time step of 0.01 s to match the time interval of the dynamic rupture simulation outputs.

5. After the perturbation ends (i.e., $t > t_u - \Delta t_g + 15$ s) keep the static stress changes:

$$\tau^0(z) = \tau^0(z) + \hat{\tau}(z, t_f)$$

$$\sigma_n^0(z) = \sigma_n^0(z) + \hat{\sigma}_n(z, t_f),$$

where $t_f = t_u - \Delta t_g + 15$ s is the final time of the perturbation period. Continue running the SEAS simulation until a system-size earthquake occurs, and record the time of this event, t_p (blue line in Fig. 3a). This model is referred to as a 'perturbed' model.

6. Calculate the time difference between the system-size earthquakes with and without the perturbation: $\Delta t = t_u - t_p$. Δt is a measure for the triggering response. A positive Δt indicates that the perturbed system-size earthquake (mainshock) occurs earlier than in the unperturbed model, indicating a clock advance. A negative Δt indicates a mainshock clock delay.

Incorporating the stress-dependent aging law (Eq. (6)) requires a slight modification during the perturbation period (i.e., step 4 above):

1. Repeat steps 1 - 3 as outlined above.
2. During the perturbation period ($t \in [t_u - \Delta t_g,\ t_u - \Delta t_g + 15$ s]), apply the stress-dependent aging law. The stressing rate during this perturbation ($\dot{\sigma_n^p}$) depends solely on the external stress perturbation ($\hat{\sigma}_n$):

$$\begin{aligned}\dot{\sigma}_n^p(z,t) &= \dot{\sigma}_n(z,t) + \dot{\hat{\sigma}}_n(z,t) \\ &= \dot{\sigma}_n^0(z) + \dot{\hat{\sigma}}_n(z,t) \\ &= \dot{\hat{\sigma}}_n(z,t)\,,\end{aligned}$$

since the background normal stress in the SEAS simulation (σ_n^0) remains constant over time (i.e., $\dot{\sigma}_n^0(z) = 0$). Then, Eq. (6) becomes:

$$\frac{d\theta}{dt} = G(\|\boldsymbol{V}\|, \theta) - \alpha \frac{\theta}{b} \frac{\dot{\sigma_n^p}}{\sigma_n^p} = G(\|\boldsymbol{V}\|, \theta) - \alpha \frac{\theta}{b} \frac{\dot{\hat{\sigma_n}}}{\sigma_n + \hat{\sigma_n}},$$

where $G(\|\boldsymbol{V}\|, \theta) = 1 - \frac{\|\boldsymbol{V}\|\theta}{D_{RS}}$. Aside from the state variable evolution law, everything else is the same as step 4 in the previously described procedure.

3. For $t > t_u - \Delta t_g + 15$ s, switch the state variable evolution law back to the aging law and keep the constant static stress change. Repeat steps 5 - 6 in the previously described procedure to obtain Δt.

3 Results

3.1 Dynamic and Static Stress Change Estimation

The 3D dynamic rupture simulations well capture the dynamics of the M_w 5.4 foreshock along the mainshock fault. Figure S4 shows examples of spatiotemporal evolutions of the ΔCFS across the mainshock fault with 340° strike, assuming different foreshock fault dips and rupture characteristics. The dynamic stress transfer mediated by body waves and reflections from the free surface is clearly observed. The peak dynamic ΔCFS values fall between 0.4 MPa and 2 MPa (Fig. S5a), consistent with the previous estimate by Z. Jin and Fialko (2020) based on a point source approximation. The static ΔCFS values range from a few kilopascals to hundreds of kilopascals (Figs. S5c-d). The sign of the static ΔCFS changes from negative in the middle of the seismogenic zone (between

5 km and 10 km) to positive at smaller depths (< 5 km) and greater depths (> 10 km), reflecting the 3D nature of the respective stress field. Detailed comparison of synthetic and observed waveforms and analysis of the sensitivity of the spatiotemporal evolution of ΔCFS to the assumed fault geometry are provided in Supplementary Section S1.

The rupture characteristics of the M_w 5.4 foreshock (Fig. 2c) mostly affect the arrival time and the amplitude of the peak dynamic ΔCFS, while having a negligible effect on the pattern of static ΔCFS (left vs. right columns of Fig. S4). We explore varying combinations of f_d and D_{LSW} to obtain two distinctive dynamic rupture characteristics that differ in their timing of the peak energy release (Fig. 2c): one set of models nucleates and releases all its energy immediately (denoted 'fast initiation' hereafter), while the others nucleate slowly, with pronounced runaway rupture initiating after 0.5 s (denoted 'slow initiation' hereafter). The slow initiation model features two distinct episodes of moment release: the first occurs after the initial, prescribed time of rupture initiation, and the second corresponds to a spontaneous transition to runaway rupture. This dynamic behavior may resemble the two subevents of the M_w 5.4 foreshock identified from apparent source time functions, separated by ∼0.8 s (Meng & Fan, 2021). In our dynamic rupture model, the first subevent releases ∼3 % of the total moment, equivalent to a M_w ∼4.4, which is small but comparable to the first observed subevent (M_w ∼4.5). The difference in moment release rate between the fast and slow initiation models is well reflected in the spatiotemporal patterns of ΔCFS. Slow initiation models show delayed arrivals of the peak dynamic ΔCFS with reduced amplitudes (Fig. S5a) compared to the fast initiation models. The reduced amplitude is likely due to a portion (∼3 %) of the total energy being released during the first subevent in the slow initiation models.

Throughout the remainder of this study, we divide the stress perturbation models into four classes defined by the combination of the foreshock fault dip and the rupture characteristics: the vertical foreshock fault and the fast initiation model (VFI), the vertical foreshock fault and the slow initiation model (VSI), the dipping foreshock fault and the fast initiation model (DFI), and the dipping foreshock fault and the slow initiation model (DSI). Therefore, we have 16 dynamic rupture models in total, combining the four model classes with four mainshock strike angles.

3.2 Triggering Responses: Aging Law

We perturb the aging law reference model (A2) following the procedure outlined in Section 2.3. We consistently obtain several hours of target mainshock clock advance ($\Delta t > 0$) for all considered cases (Fig. 4). For example, we select various target mainshocks with hypocenter depths ranging from 4.34 km to 7.82 km while fixing the stress perturbation from the VSI dynamic rupture model with 340° mainshock fault strike (denoted "VSI, 340° strike" stress perturbation model), to explore the effect of target mainshock selection on the estimated triggering response. The observed clock advance ranges from 4.5 h to 6.1 h.

Next, we apply various stress models to a fixed target mainshock (event 282 at 7.82 km depth; Fig. S3b) and observe time advances of several hours (4.1 h to 5.6 h) for all considered combinations of fault geometry and rupture characteristics of stress perturbation models. We repeat the process with different fixed target mainshocks (e.g., event 120 at 6.5 km depth; event 88 at 4.38 km depth), and the overall pattern of several hours of clock advance remains consistent.

Given the consistent behavior observed across all combinations of the perturbation model and target mainshock depths, we explore the effect of the timing of the perturbation (i.e., Δt_g). We test seven different values for Δt_g (10 yr, 1 yr, 30 h, 20 h, 16.2 h, 5 h, and 1 h) and perturb a fixed combination of the target mainshock (event 88 at 4.38 km depth) and stress perturbation model (VSI, 340° strike; Fig. 5). These Δt_g values correspond to 13 %, 1.3 %, 0.005 %, 0.003 %, 0.002 %, 0.0008 %, and 0.0001 % of the ∼76 yr

recurrence interval in the reference model. The mainshock clock is advanced for all explored timings of perturbation. The modeled Δt decreases as Δt_g decreases (Fig. 5b). However, we do not observe instantaneous triggering even when the perturbation is applied closer to the unperturbed target mainshock time (e.g., $\Delta t_g = 1$ h).

We further examine the control of Δt_g on the mainshock clock change by defining the 'closeness to instantaneous triggering' as $\Delta t/\Delta t_g$, a quantity designed to become 1 when the mainshock is triggered instantaneously (squares in Fig. S7). The closeness to instantaneous triggering varies non-linearly for different Δt_g and does not exhibit a clear trend with varying Δt_g values. This contrasts with previous simulation results with static ΔCFS perturbations showing a systematic convergence toward the instantaneous triggering curve as Δt_g decreases (e.g., Gallovič, 2008; Perfettini et al., 2003a). This implies that applying the stress perturbation later in the unperturbed earthquake cycle does not guarantee an increased possibility of instantaneous triggering, likely due to the complexity in our models.

Earthquake triggering may also depend on the amplitude of the stress perturbation (e.g., Wei et al., 2018). To explore the effect of the amplitude of the perturbing stress changes, we scale the amplitude of the VSI, 340° strike stress perturbation model by a factor ranging from 1 to 30 and perturb a given target mainshock (event 88). The amplification results in a wide range of the peak dynamic ΔCFS at the given target mainshock hypocenter location (4.38 km), from 0.5 MPa to 17.5 MPa. For smaller amplification factors (1, 2, 3, and 5), the mainshock clock is advanced but we do not observe instantaneous triggering. The magnitude of clock advance is systematically increased from 6.1 h to 11.9 h as the amplitude of the perturbing stress change increases.

The target mainshock is not triggered instantaneously, even when the stress perturbation is amplified by a factor of 10, yielding a peak dynamic ΔCFS of 5.8 MPa at the expected hypocenter depth (Fig. 6a). This peak dynamic ΔCFS value is equivalent to 27 % of the excess strength during the quasi-static nucleation ($\tau - f_0\sigma_n = 21.4$ MPa for $\sigma_n = 53$ MPa and $f_0 = 0.6$ at the nucleation site). Instead, a new partial rupture event that would not have occurred with the absence of perturbation is triggered soon after the perturbation (new event 1 in Fig. 6a), followed by a smaller partial rupture event (new event 2 in Fig. 6a), forming a new sequence that does not culminate in a system-size earthquake. A system-size earthquake occurs several months after the sequence at a slightly shallower depth, eventually delaying the time by 74 days compared to the unperturbed model. However, since the sequence that leads to the mainshock is completely altered, we do not consider the new system-sized event as a delay of the target mainshock but rather consider it as a new event not observed in the reference model.

The instantaneous triggering of a system-size earthquake occurs when the stress perturbation is amplified by a factor of 30, resulting in a peak dynamic ΔCFS of 17.5 MPa at the mainshock hypocenter depth (Fig. 6b). This peak dynamic ΔCFS value corresponds to 82 % of the excess strength during the quasi-static nucleation. We consider this event as an example of dynamic triggering since it nucleates $\sim$2.5 s after the start of perturbation, which corresponds with the arrival of the largest dynamic stress. The depth of the nucleation also matches that of the peak dynamic stress change.

In all simulations using the aging law reference model (A2), we consistently observe a mainshock clock advance. Except for the cases involving large stress perturbation amplitudes that generate entirely new foreshock sequences (Fig. 6a), the background foreshock sequences preceding the mainshock remain unchanged between perturbed and unperturbed models. Thus, the external stress perturbation from the modeled M_w 5.4 foreshock emerges as the primary driver of the observed mainshock clock change. To quantify this effect, we introduce a new metric: work per distance (W; Eq. (7), defined as the

work density integrated over the entire fault:

$$W = \int_0^{L_f} \int_0^{\Delta\delta(z)} \Delta\tau(z,\delta)\, d\delta dz, \tag{7}$$

where δ is slip, $\Delta\delta$ and $\Delta\tau$ are the net slip and shear stress changes during the perturbation period, respectively. The W metric combines the external stress perturbation and background slip and reflects the net energy transfer associated with the perturbation. This metric well captures the net energy gain or loss due to the applied stress perturbation along the fault. Although W metric includes both velocity-weakening (VW) and velocity-strengthening (VS) regions, the contribution of creep in VS regions ($V \sim 10^{-9}$ m/s) to W is minor compared to that in VW regions ($V \sim 10^{-6}$ m/s).

The proposed W metric differs from standard ΔCFS calculations in two ways. First, it incorporates background slip in the calculation (via the inner integration in Eq. (7)), accounting for the interaction between stress perturbations and the slip response of the fault. Second, it integrates this over the entire fault (outer integral in Eq. (7)), yielding a fault-averaged estimate of the energy transfer and change in closeness to failure associated with the perturbation. While W and ΔCFS yield similar implications in cases where stress changes are uniformly positive or negative, W becomes particularly useful when stress changes are heterogeneous, e.g., when different parts of a fault experience a mixture of loading and unloading. Thus, we use the W metric to provide useful insights into the closeness of failure of a fault experiencing spatial variations of stress changes.

To understand the underlying physical mechanisms, we examine the correlation of the clock advance with five key physical parameters (Fig. 4): peak dynamic ΔCFS and static ΔCFS at the depth of maximum slip during the perturbation period (i.e., at $z_{max} = \text{argmax}_z\, \delta(z)$), peak slip, peak slip rate, and W along the entire fault. We compute the Pearson correlation coefficient R between Δt and each parameter for a quantitative comparison.

The clock advances from our models show a strong correlation with both peak dynamic ΔCFS and static ΔCFS values, showing R values of 0.86 and 0.94, respectively. Both parameters show a positive, almost linear, relationship with the clock advance. However, we find that peak dynamic ΔCFS and static ΔCFS are themselves strongly correlated, with a high $R = 0.97$ (Fig. S8). This indicates that if either peak dynamic ΔCFS or static ΔCFS correlates positively with the clock advance, the other may appear correlated as well due to this interdependence. We discuss this potential confounding effect in more detail in Section 4.2.

Note that we measure both ΔCFS values at z_{max} instead of the hypocenter depth in the unperturbed models. This choice is made to fully reflect the ongoing aseismic slip at the time of perturbation in our models, mostly in the form of afterslip of the preceding foreshocks (see Fig. 8). We will discuss more about this choice in Section 4.5.

In contrast, the peak slip, the peak slip rate, and the work per distance do not show a strong correlation with the estimated clock advance ($R \leq 0.53$). However, it is worth noting that all W values are positive for all clock advance models. As will be discussed in more detail in Section 4.3, the sign of the W value effectively predicts whether the mainshock will advance or delay as a response to the given stress perturbation.

3.3 Triggering Responses: Other Evolution Laws

In the previous section, the models with aging law consistently predict the clock advance of the next large event regardless of the choice of event, stress perturbation model, and timing of perturbation, unless the amplitude of perturbing stress is significantly elevated to produce instantaneous triggering. In this section, we explore triggering responses from other state evolution laws.

Although adding the stress-dependent term in the evolution law (i.e., the last term in Eq. (6)) is expected to make the models more realistic, it is still poorly understood how this stress-dependency affects the state variable evolution on a fault with a complex seismic and aseismic slip history and in turn, how it would affect the triggering response on the fault. Thus, we estimate the triggering response with stress-dependent aging law, following the procedure outlined in Section 2.3, and compare the results with those from the aging law reference model (Section 3.2). The stress-dependent aging law and aging law reference model take the same unperturbed model (A2), but differ in that the stress-dependent term is applied during the perturbation period for the stress-dependent aging law models. We again obtain mainshock clock advances (i.e., $\Delta t > 0$) of several hours when using the stress-dependent aging law, but the Δt estimates are systematically smaller compared to the aging law reference model (Fig. 7). For example, a given combination of target mainshock (event 282 at 7.82 km depth) and the stress perturbation model (VSI, 340° strike) yields $\Delta t = 4.5$ h when using the aging law, while $\Delta t = 3.7$ h is obtained using the stress-dependent aging law (Fig. 7a). The decreased magnitude of clock advance in stress-dependent aging law is robustly obtained for all five tested cases with different target events and stress perturbation models (Fig. 7b).

The reduction of clock advance can be well explained in the framework of W. With the stress-dependent term, the evolution of the state variable and the slip rate during the perturbation period resembles that of the external stress perturbation, leaving a depth-dependent static change in both variables. Therefore, tracking the change in variable at a single depth cannot fully explain the systematic decrease in Δt. We rather compute the W values from the stress-dependent law models, which reflect integrated effect along the entire fault, and obtain systematically lower W values compared to the aging law reference models (Fig. 7c). Since models using different evolution laws are perturbing the same target mainshock using the same stress perturbation, the reduction in W originates from the amount of slip at regions under higher ΔCFS values. Integration of the state variable in Eq. (6) leads to a minor decrease in slip in the stress-dependent law models, thus causing slightly smaller advances of the time of mainshock. This result emphasizes the importance of an integrative approach to assess the effects of external stress perturbation.

Next, we explore whether using the slip law (Eq. (5), Fig. S2b) significantly alters the triggering response, since the slip law may facilitate triggering compared to the aging law owing to its smaller nucleation size (Ampuero & Rubin, 2008). We perturb the slip law reference model (S10) with different stress perturbation models and obtain a similar pattern of clock advance of several hours, ranging from 6 h to 8 h. We cannot explore the effect of hypocenter depth since the slip law reference model produces a repetitive sequence with a single hypocenter depth (6.92 km) for system-size events. The clock advance of 6 to 8 h is comparable to that of 5 to 9 h estimated from the aging law reference model using a system-size event with a similar depth of 6.5 km. However, we cannot directly compare the Δt value between the slip law reference model and the aging law reference model due to their different parameter setups.

For a better comparison, we perturb model A10 (Fig. S2c) with different stress perturbation models, and surprisingly, we consistently obtain mainshock clock delays (i.e., $\Delta t < 0$), instead of advances. To understand the key control of clock advance versus delay, we investigate the five key parameters examined in Figure 4 for both clock advance and clock delay models (Fig. S9). We observe that the static ΔCFS value and W value exhibit a clear distinction between the clock advance models and the clock delay models. All clock delay models from model A10 show negative values for both parameters, in contrast to all clock advance models, which show positive values (Figs. S9b & e). The notable contrast in the static ΔCFS value and W value implies a strong control of the combined effect of the static ΔCFS and background aseismic slip along the entire fault on the mainshock clock change. We discuss this combined effect in detail in Section 4.3.

The only deviation between the sign of W and the sign of Δt occurs when the perturbation is applied well before the target mainshock (i.e., larger Δt_g). We obtain a mainshock clock delay of $\sim$13 yr when we increase Δt_g to 30 yr, unlike the clock advances obtained from smaller Δt_g values (Fig. S10). Then, the estimated W value is very small but positive, an unexpected outcome for a model with a mainshock clock delay. Using $\Delta t_g = 30$ yr, the perturbation is applied before the first transient in a sequence of SSEs occurring in the deeper part of the seismogenic zone, preceding the target foreshock-mainshock sequence. This perturbation triggers a new SSE, which ultimately delays the target mainshock's onset. This implies that the external energy applied at $\Delta t_g = 30$ yr is insufficient to affect the nucleation of the foreshock-mainshock sequence but instead is consumed in initiating an additional aseismic transient. The unpredictable behavior associated with the complex SSE sequence emphasizes the importance of considering aseismic processes in the context of longer seismic cycle history.

In addition, we find a decrease of Δt value when using the stress-dependent aging law to perturb the A10 models. For example, we obtain 6 h of time delay (i.e., $\Delta t = -6$ h) when perturbing target mainshock 18 in model A10 using the VSI, 340° strike stress perturbation model. When assuming the stress-dependent aging law during the perturbation period, the time delay increases to 6.5 h (i.e., $\Delta t = -6.5$ h). This result suggests that the stress-dependent term systematically decreases Δt value, regardless of its sign.

4 Discussion

4.1 Lack of Instantaneous Triggering

Throughout this study, we persistently observe a lack of instantaneous triggering. In Section 3.2, we find that instantaneous triggering does not occur even for small values of Δt_g and that the proximity to instantaneous triggering is unpredictable. Some studies suggest that a larger perturbing stress amplitude leads to a more rapid convergence toward instantaneous triggering as Δt_g decreases (Gallovič, 2008; Gomberg et al., 1998; Perfettini et al., 2003a, 2003b). To analyze such amplitude dependency, we repeat the analysis detailed in Section 3.2 with a stress perturbation amplitude elevated by a factor of 5 (resulting in a peak stress change of $\sim$3 MPa at the expected target hypocenter depth; triangles in Fig. S7). As expected, the overall proximity to instantaneous triggering increases with elevated amplitudes. However, the proximity to instantaneous triggering systematically decreases with smaller Δt_g values, indicating less efficient triggering when the perturbation occurs later in the cycle. The non-monotonic response of Δt for varying Δt_g may be explained as a combined contribution from transient (larger Δt value when applied later in the cycle) and static (smaller Δt value when applied later in the cycle) stress changes, as suggested by Gomberg et al. (1998). These analyses with varying Δt_g demonstrate that the timing of the perturbation is not a crucial factor in instantaneous triggering.

In our model parameterization, instantaneous triggering occurs only when the peak amplitude of stress perturbation at the unperturbed mainshock hypocenter depth is elevated to 17.5 MPa (30-times elevated model; Fig. 6b). We identify instantaneous triggering as dynamically triggered based on the occurrence time and hypocentral depth, which coincide with the arrival of the peak dynamic ΔCFS. The amplitude required for instantaneously triggered rupture in this study (17.5 MPa) is comparable to the additional prestress level required to dynamically nucleate the Ridgecrest mainshock after the M_w 6.4 foreshock (18 MPa), estimated from a realistic sequence of 3D dynamic rupture simulations (Taufiqurrahman et al., 2023). The required peak stress change amplitude of a few tens of MPa is also consistent with the dynamic triggering threshold inferred from peak seismic velocities (Gomberg et al., 2001). This amplitude (17.5 MPa) is slightly less than, but comparable to, the steady-state-to-peak stress change of 20.4 MPa

produced by the unperturbed model. This implies that the amplitude of the stress perturbation is expected to be comparable to the excess strength during the quasi-static nucleation for an instantaneous dynamic triggering to occur. Because the excess strength scales with the effective normal stress, this may explain why dynamically triggered earthquakes are mostly observed in geothermal areas (Aiken & Peng, 2014; Brodsky & Prejean, 2005; Hirose et al., 2011; Husen et al., 2004), where the effective normal stress may be locally low due to the presence of over-pressurized fluids. The triggering stress required in the perturbed model is somewhat lower (< 90 %) compared to the strength excess, indicating that the passage of seismic waves may additionally affect the effective fault strength.

We find that a peak dynamic ΔCFS of moderately large amplitude ($\sim$5.8 MPa at the unperturbed hypocenter depth) is capable of triggering partial ruptures which alter the stress distribution along the fault, subsequently leading to an entirely new sequence of earthquakes following the perturbation (Section 3.2; Fig. 6a). From a seismic hazard perspective, the models presented here may imply that an earthquake is less likely to be triggered immediately by another earthquake unless a sufficiently high stress is applied. However, a significantly strong perturbation may affect the occurrence of smaller earthquakes, causing changes in the timing and location of nucleation of the next large earthquake in a highly non-linear, complex way.

4.2 Which is Dominant in Earthquake Triggering: Static or Dynamic Stress Changes?

Identifying the roles of static and dynamic stress changes in earthquake triggering is important for seismic hazard assessment, specifically in the aftermath of large earthquakes. We aim to understand the relative contribution of each process. So far, we present models containing both dynamic and static components of ΔCFS and provide insights into their combined impact on the mainshock clock change.

We now compare how the Δt estimates change when we perturb using only the dynamic component of the ΔCFS or only the static component. First, we separate the dynamic and static components of the ΔCFS from the VSI, 340° strike stress perturbation model by tapering out the early ($t < 10$ s) or late ($t > 10$ s) part of the computed time series of dynamic stress perturbations due to the modeled M_w 5.4 foreshock (Fig. S11).

In Figure S12, we compare the triggering response from dynamic-only and static-only models with that from the original stress perturbation model, which includes both dynamic and static components. When both components are included, we obtain a mainshock clock advance of 4.5 h. In contrast, the mainshock clock advances only by a few seconds (3.9 s) when we perturb with the dynamic-only perturbation model. The static-only perturbation model almost fully reproduces the mainshock clock advance of 4.5 h. The Δt estimates of the original model and static-only model differ by only 1.4 s. The dominance of static ΔCFS is robust when tested with different sets of target mainshocks and stress perturbation models. Thus, we conclude that static ΔCFS is more effective in altering the timing of a future mainshock in the current model setup.

The dominance of the static stress change in earthquake triggering was suggested in previous studies as well. High-precision earthquake catalogs reveal a lower triggering threshold for static stress change compared to the dynamic stress change (Gomberg et al., 2001) or a strong size-to-distance relationship of aftershocks (van der Elst & Shaw, 2015). Also, a delayed change in seismicity rate, particularly a delayed decrease in seismicity rate, can be well explained by the static stress transfer (Kroll et al., 2017; Toda et al., 2012). In numerical simulations with rate-and-state friction law, a higher triggering potential of the static ΔCFS compared to the dynamic ΔCFS of the same amplitude is reported for fast and slow earthquakes (Belardinelli et al., 2003; Gomberg et al., 1998; Luo & Liu, 2019; Yoshida et al., 2020).

The dominance of static stress changes in controlling the mainshock clock change may indicate that the positive correlation between peak dynamic ΔCFS and Δt in Figure 4a primarily reflects the strong correlation between dynamic and static stresses themselves (Fig. S8). Without explicit simulations isolating the static and dynamic components of stress changes, as done in this study, it might be easy to mistakenly attribute a comparable influence to dynamic ΔCFS. This finding highlights the need for caution when interpreting correlations in triggering studies, as apparent relationships may arise from underlying parameter interdependence.

Although our models show that static ΔCFS dominates the mainshock clock change, the use of fully dynamic foreshock simulations may provide further insights. By resolving the full spatiotemporal evolution of stress, including both static and transient components, one can assess their relative contributions within a unified framework, bearing on our conclusions about the dominance of static stress in delayed triggering.

However, the limited contribution from the dynamic ΔCFS in our models cannot fully explain the frequent observation of dynamic triggering, particularly in the far field. The lack of dynamic triggering in this study might be related to the short duration ($<$ 5 s) of the dynamic ΔCFS used in this study (Katakami et al., 2020; Wei et al., 2018). Additional weakening mechanisms that are not considered in this study, such as pore pressure changes, thermal pressurization, localization of brittle deformation, or off-fault damage, may play a crucial role in facilitating dynamic triggering (e.g., Brodsky et al., 2003; Elkhoury et al., 2006; Gabriel et al., 2024; Zhu et al., 2020).

Another mechanism that may contribute to the complexity of earthquake triggering is the cumulative stress transfer from multiple foreshocks. We observe a systematic shortening of the duration of the modeled cascading foreshock-mainshock sequence as a result of perturbation. For example, the duration of the foreshock-mainshock sequence (i.e., time from the leading foreshock to the system-size earthquake) in one of the sequences in the unperturbed aging law reference model is 1166 s, which becomes 411 s when it is perturbed (Fig. S13). Similar behavior has been shown in models with a rough fault surface, where creep was accelerated in areas of low effective normal stress due to foreshocks (Cattania & Segall, 2021). This shortening of the sequence implies that the superposition of perturbations from multiple foreshocks might significantly advance the mainshock occurrence time. While this study only considers the stress changes inferred from the closest M_w 5.4 foreshock, the 2019 Ridgecrest mainshock was accompanied by multiple foreshocks, including the largest M_w 6.4 foreshock (e.g., Meng & Fan, 2021; Ross et al., 2019; Shelly, 2020). Although a single foreshock's perturbation may not be sufficient to dynamically trigger the mainshock, it might be possible to dynamically trigger the mainshock if the fault is sufficiently weakened due to prior seismicity.

4.3 What Controls the Mainshock Clock Change?

We investigate the dominant factors controlling the sign of the Δt estimate in the models presented here. First, to confirm that the mainshock clock change in the complex sequences of seismic and aseismic events cannot be fully explained by a simple analytic solution, we compare the change in time to instability (defined as $t_i = \Delta t_g - \Delta t$) measured from our simulations to that derived for a 1D spring-slider solution (Fig. S14; Eq. (A11) in Dieterich, 1994). We do not follow this formula (Eq. (A11) in Dieterich, 1994), but rather adopt the concept that an increase in stress may lead to an increase in slip rate and a reduction of the time to instability, acknowledging that the complex model setup in this study and the 1D spring slider solution are not directly comparable.

We apply the perturbation at $t_i = 16.2$ h before the target mainshock (event 282) using the VSI, 340° strike stress perturbation model. After the perturbation, we measure a t_i of 11.7 h. The perturbation causes a quasi-constant increase in the slip rate of

4.8×10^{-8} m/s. Tracking the time in the unperturbed model when this increased slip rate is reached yields a much shorter time to instability (t_{D94}) of 2.7 h. The deviation of time to instability from the analytical solution has been documented for complex models, particularly for those involving a rheological transition from VW to VS (Kaneko & Lapusta, 2008), agreeing well with our models with multiple VW-to-VS transitions along the fault (Fig. S1c). The large discrepancy between these two estimates indicates that simple analytic solutions may not be suitable for predicting the triggering response on natural faults with complex earthquake and slow-slip transient history.

To discuss the question of what may control the mainshock clock change on a complex fault, we compare models that show clock advance and clock delay (Fig. 8). The clock advance and delay are obtained by perturbing target mainshocks at similar hypocentral depths of 4.38 km and 3.7 km in models A2 and A10, respectively, using the same stress perturbation (VSI, 340° strike). The perturbed A2 model yields a clock advance of 6 h (Fig. 8a), while the perturbed A10 model yields a mainshock clock delay of 6 h (Fig. 8b).

The key difference between these two cases lies in the depth extent of the ongoing aseismic slip at the time of the perturbation. The clock delay model shows a wider zone of aseismic slip ranging from ∼7 km to 15 km (Fig. 8b), while the clock advance model shows a narrower zone of aseismic slip confined near ∼11 km depth (Fig. 8a). This difference arises from the month-long foreshock sequence in the A10 model, although the two models share the same Δt_g of 16.2 h.

We recall that the static stress shadow occurs between 5 km and 10 km depth, overlapping with the depth extent of the aseismic slip in the clock delay model but not in the clock advance model (Fig. 8b). Since the perturbation does not induce significant slip, the ongoing aseismic slip controls the net amount of work done by each fault (i.e., δ in Eq. (7)). In all of our models, if the fault slips within the static stress shadow, W is negative, delaying the next earthquake (Fig. S9e). Conversely, in the clock advance model, W is positive, promoting the onset of the next earthquake. To probe the robustness of this behavior, we perturb the same event (event 88 at 4.38 km) in the aging law reference model with a much smaller Δt_g of 2 min, the time at which the afterslip from foreshocks is extended to the static stress shadow. Despite the proximity to the unperturbed event time, we observe a clock delay of 82 s, accompanied by a negative W value.

We conduct additional sets of simulations to verify that these correlations between positive W and clock advance are not dependent on the specific choice of parameters used in this study. We test four additional reference SEAS models (Supplementary Section S2), incorporating either a lower loading velocity (Fig. S15a) or fractal heterogeneities with varying length scales (Figs. S15b-c) and amplitudes (Fig. S15d). These reference models produce foreshock-mainshock sequences with different recurrence intervals (e.g., from ∼76 yr under higher V_{pl} to ∼1915 yr under lower V_{pl}) and/or varying hypocenter depth distributions. Across a range of target mainshocks in these four models and different stress perturbations, we find several minutes to hours of clock advance when W is positive, whereas we obtain several days of time delay when W is negative. Thus, we conclude that the control of the sign of the static ΔCFS under regions of active aseismic slip on the mainshock clock advance and delay is not restricted to the specific set of parameters used in Section 3.

We find that the change in the mainshock clock is mostly controlled by the aseismic transfer of energy instead of the direct change from the perturbation itself. We explore how the stress perturbation changes the fault friction evolution by plotting a phase diagram (Belardinelli et al., 2003; Dublanchet et al., 2013; Rice & Tse, 1986). Figure 9 shows the phase diagram of a scenario perturbing the target mainshock event 282 in model A2 (Fig. S3b) using the VSI, 340° strike stress perturbation model. We find that the fault is neither significantly brought closer to nor farther from the steady state during the per-

turbation period (pink lines in Fig. 9). Instead, the perturbed evolution curve deviates from the unperturbed evolution curve before the start of the foreshock-mainshock sequence (i.e., shallow SSE period; Fig. 9a) and during the foreshocks (Figs. 9b-c). During the mainshock, however, the evolution of friction in the perturbed and unperturbed models appears comparable (Fig. 9d). We observe similar behavior across different depths, including shallow and deep creeping patches (Figs. S16a-c), and in multiple scenarios, including the same target mainshock (event 282) and stress perturbation (VSI, 340° strike) pair modeled with the stress-dependent friction law and the clock delay case (Figs. S16d-f). In all cases, the perturbed and unperturbed models show a similar frictional evolution during each mainshock, indicating that the perturbation has little impact on the mainshock dynamics. The phase diagram suggests that the effect of external stress perturbations on the frictional evolution of a mainshock is insignificant, as most of the stress changes are accommodated by aseismic slip and foreshocks. This stress adjustment alters the duration of preceding foreshocks or aseismic transients (Fig. S13), leading to a change in the mainshock timing.

External stress perturbations may alter the energy budget of a fault and its slip distribution. This effect is amplified in regions undergoing accelerating slip, such as afterslip or SSEs, where small stress changes may result in large changes in slip and energy release. In contrast, regions experiencing low slip rates respond less efficiently. The response to perturbation in our models is fundamentally shaped by both internal dynamics and external forcing. A change in the fault's energy budget in turn affects the characteristics of foreshocks and aseismic slip, as illustrated in the phase diagrams in Figures 9 & S16. This explains why the work-per-distance metric W, which integrates the fault-averaged change in energy budget and stress-slip interaction, is a good indicator of the sign of the mainshock clock change.

These results highlight the crucial role of the interaction between external stress perturbations and ongoing background slip in earthquake triggering in complex earthquake sequences with realistic stress perturbations. The contribution of aseismic processes on earthquake triggering has also been suggested by previous studies (e.g., Cho et al., 2009; Gallovič, 2008; Inbal et al., 2023; Kostka & Gallovič, 2016).

4.4 Implications for the 2019 Ridgecrest Earthquake Sequence

The model results presented in this study, together with previous studies, may provide insights into key features observed in the 2019 Ridgecrest sequence. The W metric introduced here supports previous inferences that the M_w 6.4 foreshock may have brought the mainshock fault closer to failure (e.g., Barnhart et al., 2019; S. Li et al., 2020; Taufiqurrahman et al., 2023). Previous models show a ΔCFS increase due to the M_w 6.4 foreshock at all depths near the Ridgecrest mainshock hypocenter (e.g., Magen et al., 2020; Taufiqurrahman et al., 2023; Wang et al., 2020). Within the framework of W, this uniform increase in ΔCFS results in a positive W value regardless of the depth extent of background aseismic slip, likely advancing the clock of the mainshock rupture.

The analysis with varying Δt_g in Section 3.2 supports the idea that the mainshock fault was on the verge of runaway rupture at the time of the M_w 5.4 foreshock. For $\Delta t_g =$ 30 h (pink line in Fig. 5), the model yields $t_i = \sim$15 h, comparable to the observed 16.2 h interval between the M_w 5.4 foreshock and the mainshock. This Δt_g value corresponds to 0.005 % of the $\sim$76 yr recurrence interval, suggesting the M_w 5.4 foreshock occurred in the final stage of the mainshock fault cycle.

Despite the mainshock fault being near failure, the M_w 5.4 foreshock did not immediately trigger a runaway rupture. This may be resembled by the lack of instantaneous triggering in our models, where realistic stress perturbation amplitudes fail to immediately trigger the mainshock, regardless of the source characteristics of the foreshock. Based

on these results, a plausible explanation for the non-immediate triggering of the M_w 5.4 foreshock may be the insufficient amplitude of the stress perturbation.

In addition, the analysis of models with different stress perturbation amplitudes (Section 3.2) may provide insight into why the M_w 7.1 mainshock occurred on a relatively quiet fault. In Section 3.2, we show that moderately large stress perturbations can trigger multiple partial ruptures that are not present in the unperturbed sequence (Fig. 6a). Based on this result, we suspect that, if the M_w 6.4 foreshock imposed a large stress change relative to the quasi-static strength of the mainshock fault, it could have triggered additional foreshocks that would not have occurred otherwise. These triggered foreshocks might have cumulatively shortened the mainshock's recurrence interval (e.g., Fig. S13), resulting in an earlier M_w 7.1 mainshock rupture.

However, the primary goal of this study is to gain general insights into (delayed) earthquake triggering, rather than to reproduce the full details of the 2019 Ridgecrest earthquake sequence. The SEAS models used in this study assume a 1D fault under antiplane strain approximation and therefore do not capture possible along-strike variations. While our approach captures the vertical variation of stress perturbations using a 1D profile beneath the mainshock epicenter, future studies may explore along-strike variations in stress changes using fully 2D receiver fault models in a 3D domain. This would enable a more complete assessment of the triggering potential in geometrically complex fault systems.

4.5 Implications for Earthquakes within Stress Shadows

Classic Coulomb failure theory (e.g., Reasenberg & Simpson, 1992) predicts that 'stress shadows' (Harris & Simpson, 1996, 1998) move faults away from failure. However, numerous aftershocks, including large-magnitude events, occur within these regions (Felzer & Brodsky, 2005; Hori & Kaneda, 2001), complicating seismic hazard assessment. Several mechanisms have been suggested to explain these earthquakes occurring within a stress shadow region, including dynamic stress transfer, errors in Coulomb stress change calculations, rapid stress relaxation, and small-scale heterogeneities in background stress or fault geometry (Hardebeck & Harris, 2022; Hill et al., 1993; Hori & Kaneda, 2001; Marsan, 2006).

In this study, static ΔCFS values due to the M_w 5.4 foreshock are often negative at the target mainshock hypocenter depth in the unperturbed models, even in cases where the mainshock clock advance (Fig. S17).

These modeled mainshock clock advances within stress shadows are driven by stress transfer from foreshock sequences and/or aseismic slip. We show that the mainshock clock is largely controlled by the net energy gain or loss across the slipping fault due to external stress perturbations (W), governed by complex stress-slip interaction across different parts of the fault (Section 4.3). Even when a hypocenter locally experiences negative ΔCFS, the interplay between background aseismic slip and external stress perturbations could promote an earthquake, if the entire fault gained energy under the external stress perturbation. This mechanism may account for earthquakes occurring within stress shadows.

In addition, since both background aseismic slip and external stress perturbations are highly depth-dependent (Fig. 8), focusing on a specific depth to assess the triggering potential might be misleading. We suggest that evaluating the response of the entire fault (e.g., through W analysis) may be required. Unfortunately, this is problematic in the case of natural faults, since a detailed knowledge of the in situ distribution of rate-and-state friction parameters is not readily available. This presents a significant challenge for deterministic models of earthquake triggering.

5 Conclusions

We combine dynamic rupture simulations and SEAS simulations to estimate the triggering response of the 2019 M_w 7.1 Ridgecrest mainshock to the stress perturbation from the M_w 5.4 foreshock. Detailed spatiotemporal stress changes near the mainshock nucleation site are computed using 3D dynamic rupture simulations, accounting for various fault geometries (mainshock fault strike and foreshock fault dip) and foreshock rupture dynamics.

Perturbing the SEAS models using the dynamic and static stress changes from the dynamic rupture simulations consistently results in a mainshock clock advance of several hours in most cases. Aging and slip law models show comparable mainshock clock advances, while stress-dependent aging law models exhibit a systematic reduction in clock advance.

Instantaneous triggering occurs only when the peak ΔCFS at the unperturbed hypocenter depth is increased to 17.5 MPa, comparable to excess strength during the quasi-static nucleation. The timing of the perturbation has little impact on instantaneous triggering or the mainshock clock change. In some cases, triggering is less efficient when the perturbation is applied later in the cycle.

We find a dominant influence of static ΔCFS on the mainshock clock change. Models perturbed using only the static component of stress change closely reproduce the mainshock clock change seen in models with both dynamic and static components. In contrast, the dynamic ΔCFS component alone results in a minor clock advance of only a few seconds.

We explain the mainshock clock advance and delay across all explored cases by the sign of the static ΔCFS in areas of accelerating slip, quantified by the W metric. Additionally, we find that a mainshock can be promoted if the entire fault gains energy under the stress perturbation (i.e., positive W), even when the future mainshock hypocenter depth is in a local static stress shadow. This is driven by a complex stress transfer from foreshock sequences and/or aseismic slip, suggesting a possible mechanism for earthquakes occurring within stress shadows

Finally, we infer that the M_w 6.4 foreshock of the 2019 Ridgecrest sequence likely moved the mainshock fault significantly closer to failure, based on the positive W value expected from the uniform increase of ΔCFS near the Ridgecrest mainshock hypocenter.

These results highlight the critical role of foreshock sequences and aseismic deformation in earthquake triggering and emphasize the importance of considering the physics of fault-system-wide, short- and long-term processes when assessing triggering potential.

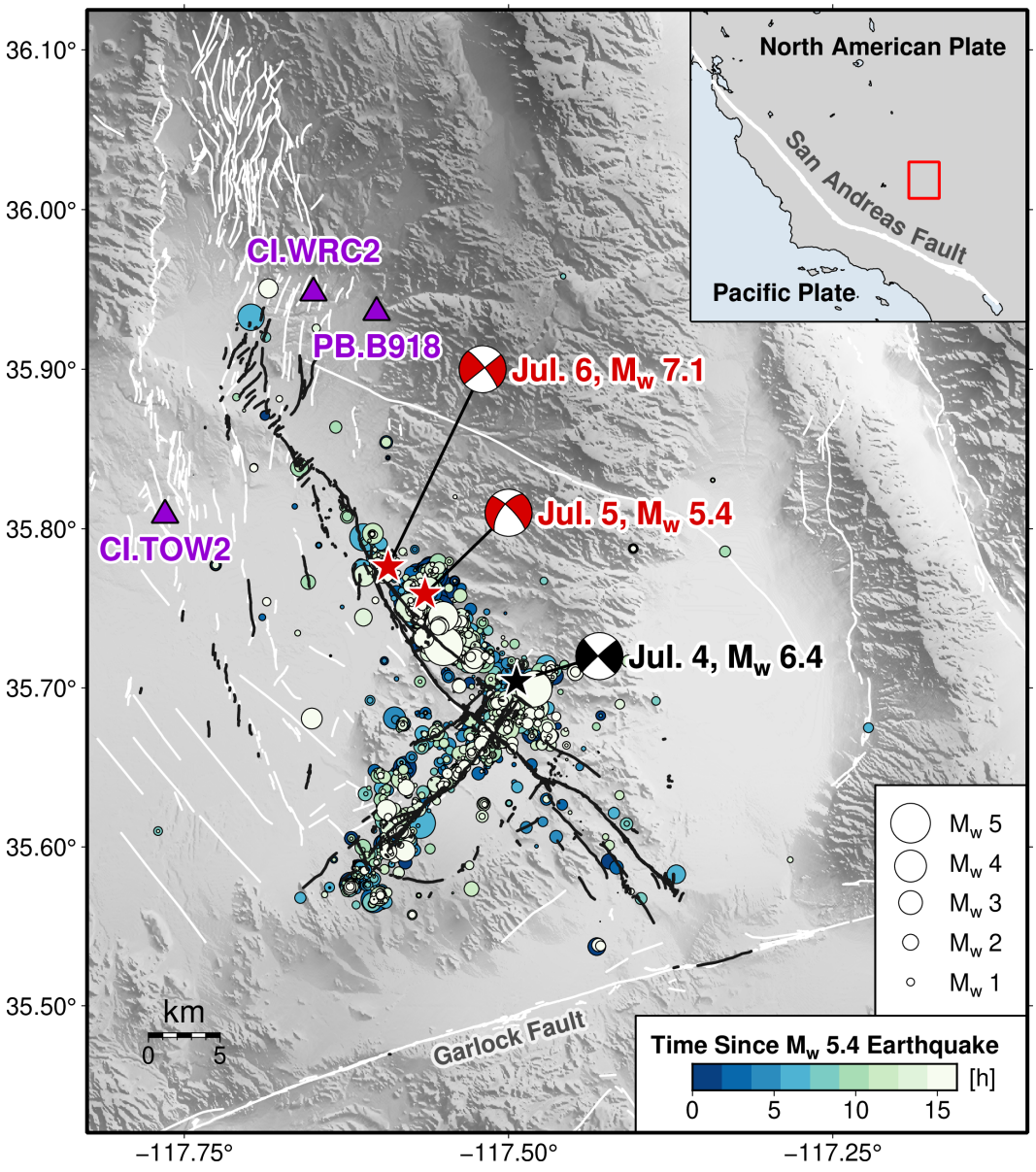

Figure 1. Regional map of the study area. The stars and beachballs indicate the epicenter locations (USGS, 2017) and focal mechanisms (SCEDC, 2013), respectively, of the M_w 7.1 mainshock (red) and the two largest foreshocks (the M_w 6.4 foreshock in black and the M_w 5.4 foreshock in red). Circles indicate epicenter locations of the seismicity between the M_w 5.4 foreshock and the M_w 7.1 mainshock (Ross et al., 2019), colored in time since the M_w 5.4 foreshock and sized by the magnitude. Black lines show surface rupture of the M_w 7.1 mainshock, and white lines indicate known Quaternary faults (USGS, 2020). Purple triangles indicate the locations of the near-field stations used for waveform comparison in Figure S6.

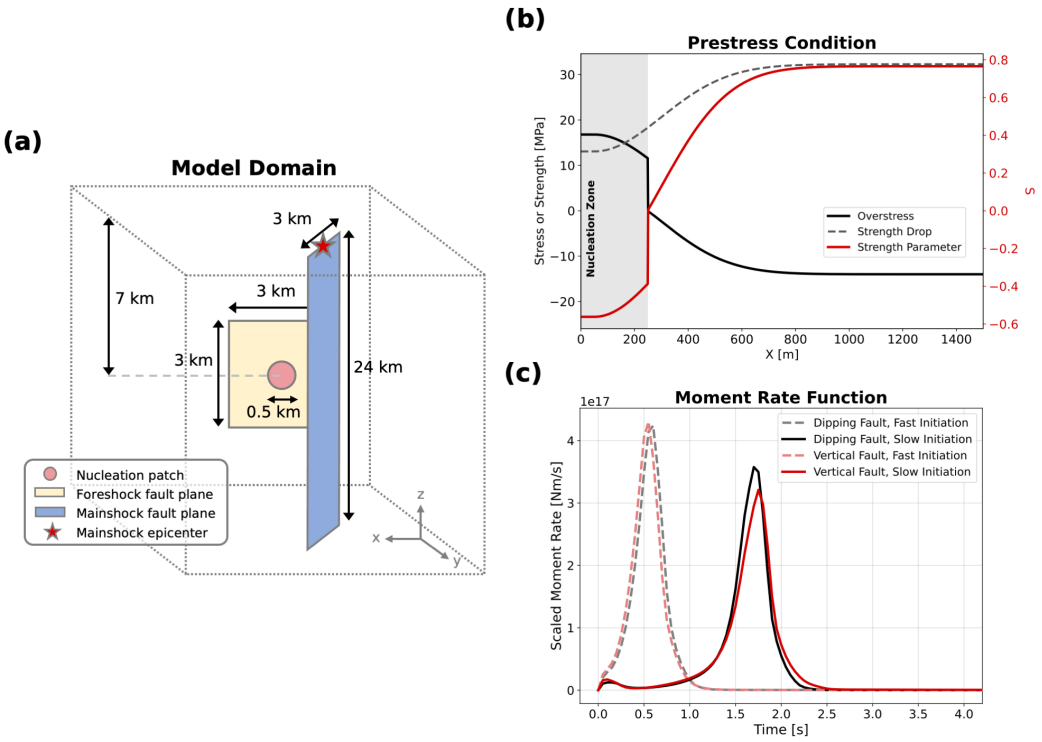

Figure 2. (a) Sketch of the model geometry for the 3D dynamic rupture simulation using *SeisSol*. The foreshock fault (yellow), mainshock fault (blue), and circular nucleation patch (pink) are shown. The red star denotes the location of the 2019 M_w 7.1 Ridgecrest mainshock epicenter. The sketch is not to scale with respect to depth (the z-axis). (b) An example of the prestress conditions used to nucleate the M_w 5.4 foreshock in the vertical foreshock fault and the slow initiation (VSI) model. The overstress (black line), the relative strength parameter S (Eq. (2); red line), and the strength drop (grey dashed line) are shown along a profile across the foreshock plane from its center to its edge. The grey shaded area indicates the extent of the nucleation patch. (c) Moment rate functions for the four classes of dynamic rupture models, classified by the combination of rupture characteristics (dashed lines for fast initiation and solid lines for slow initiation) and the dip of the foreshock fault (red hues for vertical foreshock fault and black hues for dipping foreshock fault). The moment rates are scaled by the expected moment from an M_w 5.4 earthquake (i.e., $M_{5.4}$ in Section 2.1).

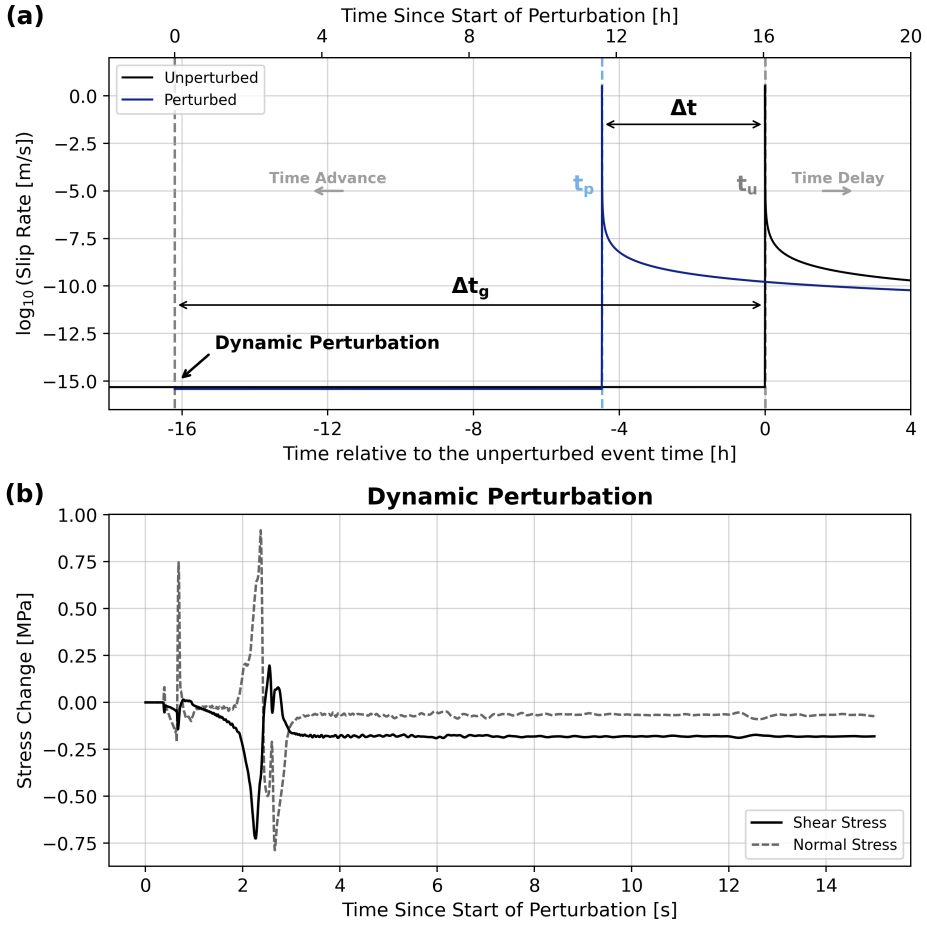

Figure 3. Illustration of the process for estimating the triggering response (Section 2.3). (a) Slip rate evolution of the unperturbed model (black) and the perturbed model (dark blue) at the mainshock hypocenter depth in the unperturbed model (7.82 km). Grey and light blue dashed lines indicate the time of the unperturbed (t_u) and perturbed (t_p) system-size earthquakes, respectively. The vertical arrow marks the timing of the applied dynamic perturbation, while the horizontal arrows represent the clock advance (Δt) and the time interval between the perturbation and the unperturbed mainshock time (Δt_g). (b) The applied dynamic stress changes at the depth of the unperturbed target mainshock hypocenter. The solid line represents the change in shear stress ($\hat{\tau}$), while the dashed line shows the change in normal stress ($\hat{\sigma_n}$). This example is generated by perturbing target mainshock event 282 (Fig. S3b) in the reference aging law SEAS model using the dynamic stress perturbation from the dynamic rupture model with the vertical foreshock fault, slow initiation (VSI) with 340° strike orientation of the mainshock fault.

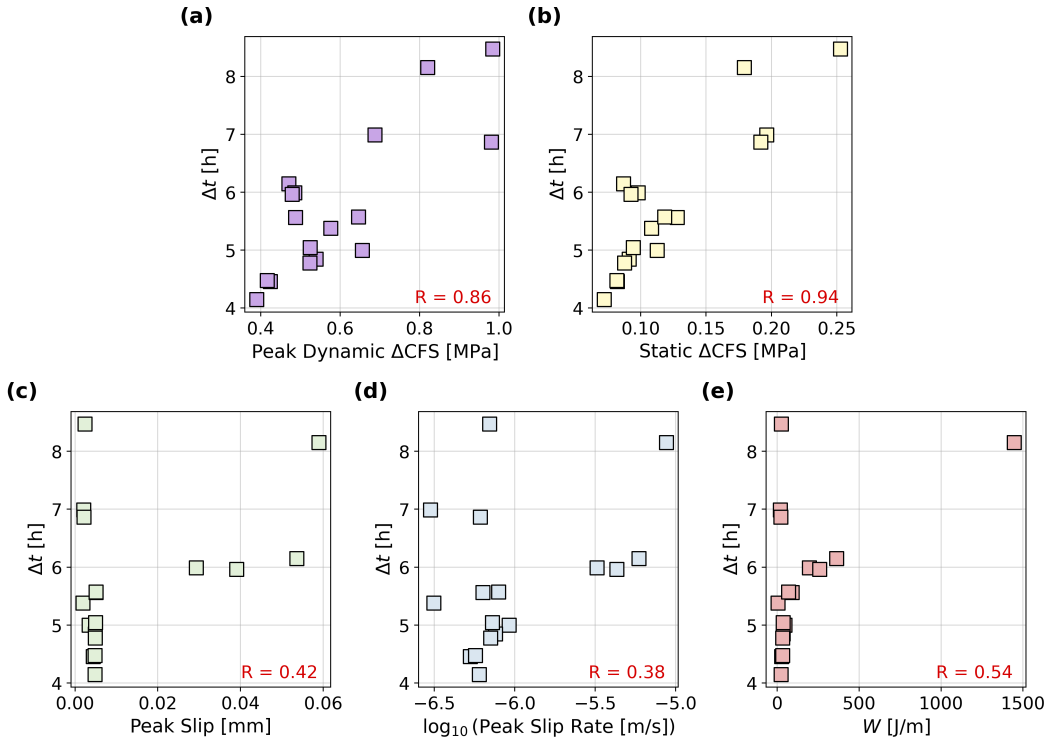

Figure 4. Correlation between the mainshock clock change (Δt) and various physical parameters obtained from all explored cases with the aging law reference model: (a) peak dynamic ΔCFS, (b) static ΔCFS, (c) peak slip, (d) peak slip rate, and (e) work per distance, W (Eq. (7)). All five parameters are estimated during the 15 s perturbation period. The ΔCFS values are measured at a depth corresponding to the maximum aseismic slip during the perturbation period in each simulation (i.e., z_{max}), while the other three parameters are measured along the entire fault. The Pearson correlation coefficient R is shown in the bottom right corner of each panel.

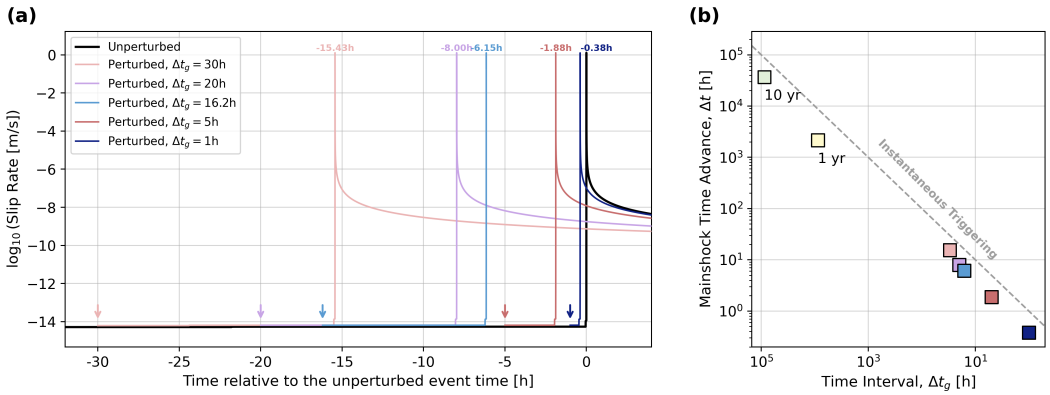

Figure 5. Comparison of triggering responses for different perturbation timings (Δt_g). (a) Slip rate at the mainshock hypocenter depth in the unperturbed model (4.38 km), for varying Δt_g values, ranging from 10 yr (light green) to 1 h (dark blue). Vertical arrows mark the timing of the applied dynamic perturbation for each Δt_g. (b) Relationship between the mainshock clock change (Δt) and the timing of perturbation. The grey dashed line indicates the expected Δt values for instantaneous triggering. Panels (a) and (b) share the same color scheme for each Δt_g. These examples are generated by perturbing target mainshock event 88 (4.38 km; Fig. 8a) in the reference aging law SEAS model using the stress perturbation from the dynamic rupture model with a vertical foreshock fault, slow initiation (VSI), and a 340° strike orientation of the mainshock fault.

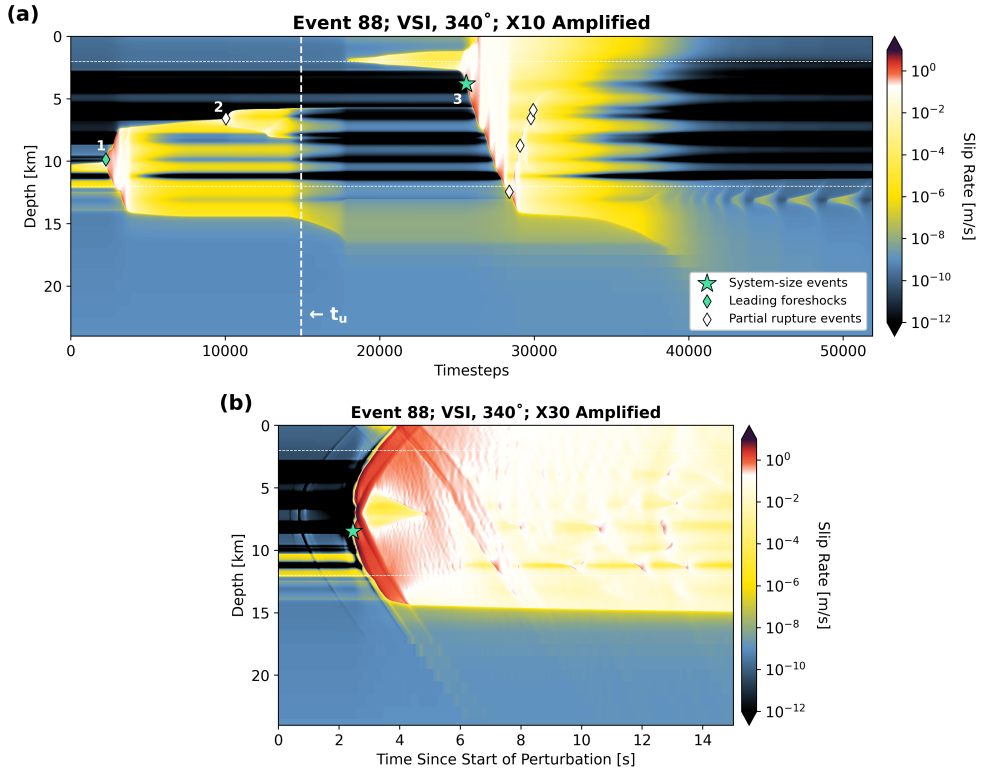

Figure 6. Spatiotemporal evolution of slip rate after applying stress perturbations with scaled amplitudes. (a) Result of the 10-times amplified stress model, where new events 1 and 2 occur 22 min and 1.6 h after the initiation of the perturbation, respectively. A new system-size earthquake (new event 3) occurs approximately 74 days later than the target mainshock in the unperturbed model. (b) Result of the 30-times amplified stress model, where a system-size earthquake is triggered $\sim$ 2.5 s after the start of the perturbation. Green stars, green diamonds, and white diamonds indicate the hypocenter locations of system-size earthquakes, leading foreshocks, and partial rupture events, respectively. Both stress perturbation models are scaled versions of the stress perturbation from the dynamic rupture model with a vertical foreshock fault, slow initiation (VSI), and a 340° strike orientation of the mainshock fault. These examples are generated by perturbing target mainshock event 88 (4.38 km; Fig. 8a) in the reference aging law SEAS model.

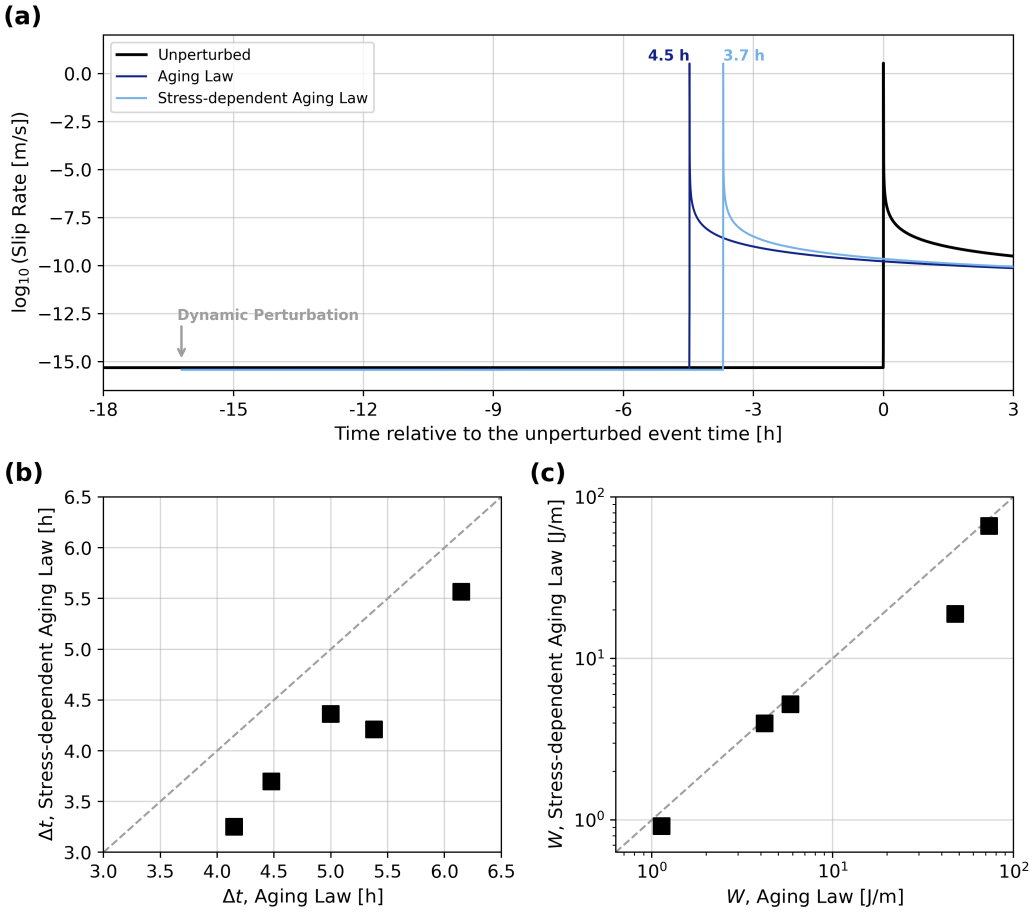

Figure 7. Comparison of SEAS models using the aging law (Eq. (4)) versus the stress-dependent aging law (Eq. (6)) during the perturbation period. (a) Slip rate at the mainshock hypocenter (7.82 km) in the unperturbed model (black) and perturbed models with the aging law (dark blue) and the stress-dependent aging law (light blue). This example perturbs target event 282 in the reference aging law SEAS model (Fig. S3b) using a dynamic rupture model with vertical foreshock fault, slow initiation (VSI), and 340° strike orientation of the mainshock fault. (b-c) Comparison of the (b) mainshock clock changes (Δt) and (c) the work per distance values (W, Eq. (7)) produced by both models. The grey dashed lines in both panels indicate a 1-to-1 relationship. Systematically smaller Δt and W values are obtained when using the stress-dependent aging law.

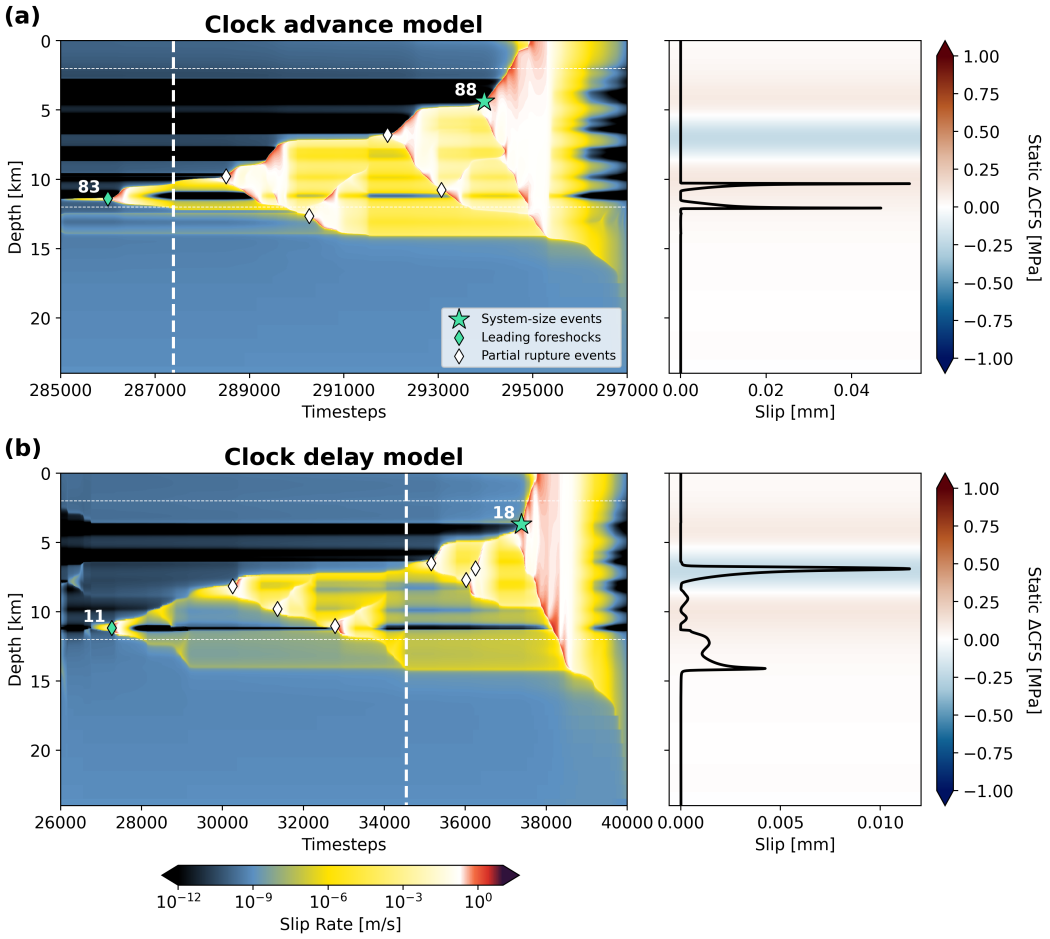

Figure 8. Comparison of the spatiotemporal evolution of slip rate for models with (a) mainshock clock advance (aging law reference model, target mainshock event 88) and (b) mainshock clock delay (model A10, target mainshock event 18). Both models are perturbed using the same stress perturbation (VSI, 340° strike mainshock fault orientation). The white dashed line in both panels indicates the time when the dynamic perturbation is applied. Green stars, green diamonds, and white diamonds indicate the hypocenter locations of system-size earthquakes, leading foreshocks, and partial rupture events, respectively. The right column shows the net slip during the 15-second-long perturbation period for each model, overlaying the static ΔCFS distribution along the fault. In the clock advance model (panel a), the maximum slip during the perturbation period occurs predominantly under positive static ΔCFS, while in the clock delay model (panel b), it occurs predominantly in the static stress shadow. (VSI: vertical foreshock fault, slow initiation.)

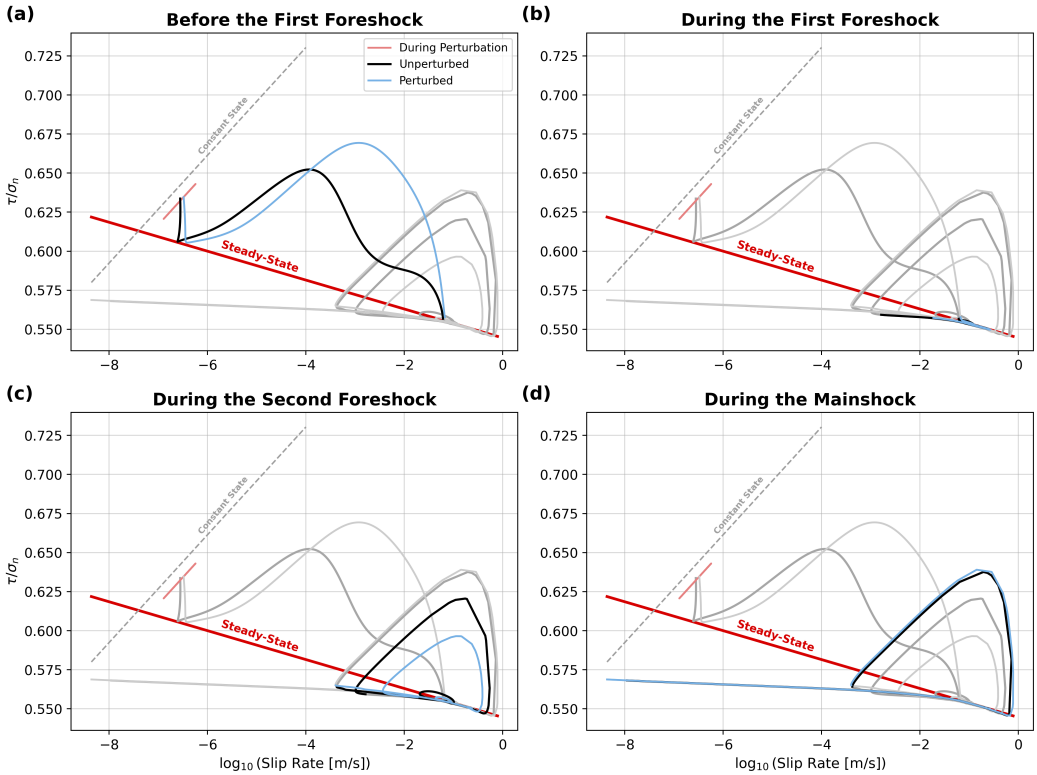

Figure 9. Phase diagram comparing the evolution of friction (shear stress over normal stress) as a function of slip rate for unperturbed model (black) and perturbed model (blue). The scenario perturbs event 282 in the aging law reference model (Fig. S3b) using the stress perturbation from the dynamic rupture model with a vertical foreshock fault, slow initiation (VSI), and a 340° strike orientation of the mainshock fault. For clarity, the diagram is divided into four stages: (a) before the first foreshock when shallow SSEs are dominant, (b) during the first foreshock (event 280 in Fig. S3b), (c) during the second foreshock (event 281 in Fig. S3b), and (d) during the system-size earthquake (i.e., mainshock, event 282 in Fig. S3b). The red solid line indicates the steady state, and the grey dashed line indicates the constant state variable contour. The incomplete cycle in panel (a) represents the shallow SSEs preceding the foreshock-mainshock sequence while panels (b) through (d) show well-developed limiting cycles of each earthquake. Friction and slip rate are measured at a depth corresponding to the maximum aseismic slip during the perturbation period (z_{max} = 3.44 km). This depth corresponds to velocity-weakening behavior. Phase diagram across different depths are shown in Figure S16.

6 Open Research

All input data required for reproducing all models are made available (Yun et al., 2025b). All dynamic rupture simulations were conducted using the open-source software SeisSol (Gabriel et al., 2025), using commit tag #e6ef661 in the master branch. All SEAS simulations were conducted using the open-source software Tandem (Uphoff et al., 2022). We used dmay/seas-checkpoint branch (commit #1dc36db) of Tandem for aging law simulations and jyun/state-law branch (commit #5d5c63f) of Tandem for slip law simulations. The location, timing, focal mechanism, and waveforms of the 2019 Ridgecrest mainshock and foreshocks were retrieved from the U.S. Geological Survey Advanced National Seismic System Comprehensive Earthquake Catalog (ANSS ComCat) (USGS, 2017) and Southern California Earthquake Data Center (SCEDC, 2013). We used the relocated earthquake catalog for the 2019 Ridgecrest earthquake by Ross et al. (2019) to plot seismicity in Figure 1. Quaternary fault traces were retrieved from the U.S. Geological Survey's Quaternary Fault and Fold Database of the United States (USGS, 2020).

Acknowledgments

We thank Editor Rachel Abercrombie, the Associate Editor, and two anonymous reviewers for their positive evaluation and constructive comments. We thank Prithvi Thakur, Camilla Cattania, and Junle Jiang for sharing their SEAS codes. We appreciate fruitful discussions with Eric Dunham. YF acknowledges support from NSF (EAR-1841273) and NASA (80NSSC22K0506). AAG and DAM acknowledge support from NSF, grants EAR-2121568 (MTMOD) and OAC-2311208 (Quakeworx). AAG acknowledges support from NSF, grants OAC-2139536 (LCCF-CSA) and EAR-2225286 (CRESCENT), the Southern California Earthquake Center (SCEC awards 24103, 24127, 22135, 23121, 22162), the European Union's Horizon 2020 Research and Innovation Programme (TEAR, grant number 852992), Horizon Europe (ChEESE-2P, grant number 101093038, DT-GEO, grant number 101058129, and Geo-INQUIRE, grant number 101058518), and NASA (80NSSC20K0495). We gratefully acknowledge the computing resources provided by the Institute of Geophysics of LMU Munich (Oeser et al., 2006). We also acknowledge the Gauss Center for Supercomputing e.V. (`https://www.gauss-centre.eu/`) for providing computing time on SuperMUC-NG, hosted at the Leibniz Supercomputing Center (`https://www.lrz.de/`), via project pn49ha.

References

Ader, T. J., Lapusta, N., Avouac, J.-P., & Ampuero, J.-P. (2014). Response of rate-and-state seismogenic faults to harmonic shear-stress perturbations. *Geophysical Journal International*, *198*(1), 385–413.

Aiken, C., & Peng, Z. (2014). Dynamic triggering of microearthquakes in three geothermal/volcanic regions of California. *Journal of Geophysical Research: Solid Earth*, *119*(9), 6992–7009.

Ampuero, J.-P., & Rubin, A. M. (2008). Earthquake nucleation on rate and state faults – Aging and slip laws. *Journal of Geophysical Research: Solid Earth*, *113*(B1).

Andrews, D. (1976). Rupture velocity of plane strain shear cracks. *Journal of Geophysical Research*, *81*(32), 5679–5687.

Árnadóttir, T., Geirsson, H., & Einarsson, P. (2004). Coseismic stress changes and crustal deformation on the Reykjanes Peninsula due to triggered earthquakes on 17 June 2000. *Journal of Geophysical Research: Solid Earth*, *109*(B9).

Atkinson, B. K. (1984). Subcritical crack growth in geological materials. *Journal of Geophysical Research: Solid Earth*, *89*(B6), 4077–4114.

Barbot, S., Fialko, Y., & Bock, Y. (2009). Postseismic deformation due to the Mw 6.0 2004 Parkfield earthquake: Stress-driven creep on a fault with spatially variable rate-and-state friction parameters. *Journal of Geophysical Research:*

Solid Earth, *114*, B07405.

Barnhart, W. D., Hayes, G. P., & Gold, R. D. (2019). The July 2019 Ridgecrest, California, earthquake sequence: Kinematics of slip and stressing in cross-fault ruptures. *Geophysical Research Letters*, *46*(21), 11859–11867.

Belardinelli, M. E., Bizzarri, A., & Cocco, M. (2003). Earthquake triggering by static and dynamic stress changes. *Journal of Geophysical Research: Solid Earth*, *108*(B3).

Belardinelli, M. E., Cocco, M., Coutant, O., & Cotton, F. (1999). Redistribution of dynamic stress during coseismic ruptures: Evidence for fault interaction and earthquake triggering. *Journal of Geophysical Research: Solid Earth*, *104*(B7), 14925–14945.

Biemiller, J., Gabriel, A.-A., & Ulrich, T. (2022). The dynamics of unlikely slip: 3D modeling of low-angle normal fault rupture at the Mai'iu fault, Papua New Guinea. *Geochemistry, Geophysics, Geosystems*, *23*(5), e2021GC010298.

Boettcher, M., & Marone, C. (2004). Effects of normal stress variation on the strength and stability of creeping faults. *Journal of Geophysical Research: Solid Earth*, *109*(B3).

Bosl, W., & Nur, A. (2002). Aftershocks and pore fluid diffusion following the 1992 Landers earthquake. *Journal of Geophysical Research: Solid Earth*, *107*(B12), ESE–17.

Brodsky, E. E., & Prejean, S. G. (2005). New constraints on mechanisms of remotely triggered seismicity at Long Valley Caldera. *Journal of Geophysical Research: Solid Earth*, *110*(B4).

Brodsky, E. E., Roeloffs, E., Woodcock, D., Gall, I., & Manga, M. (2003). A mechanism for sustained groundwater pressure changes induced by distant earthquakes. *Journal of Geophysical Research: Solid Earth*, *108*(B8).

Caskey, S., & Wesnousky, S. (1997). Static stress changes and earthquake triggering during the 1954 Fairview Peak and Dixie Valley earthquakes, central Nevada. *Bulletin of the Seismological Society of America*, *87*(3), 521–527.

Cattania, C., & Segall, P. (2021). Precursory slow slip and foreshocks on rough faults. *Journal of Geophysical Research: Solid Earth*, *126*(4), e2020JB020430.

Cho, I., Tada, T., & Kuwahara, Y. (2009). Stress triggering of large earthquakes complicated by transient aseismic slip episodes. *Journal of Geophysical Research: Solid Earth*, *114*(B7).

Day, S. M., Dalguer, L. A., Lapusta, N., & Liu, Y. (2005). Comparison of finite difference and boundary integral solutions to three-dimensional spontaneous rupture. *Journal of Geophysical Research: Solid Earth*, *110*(B12).

DeSalvio, N. D., & Fan, W. (2023). Ubiquitous earthquake dynamic triggering in southern California. *Journal of Geophysical Research: Solid Earth*, *128*(6), e2023JB026487.

Dieterich, J. H. (1979). Modeling of rock friction: 1. Experimental results and constitutive equations. *Journal of Geophysical Research: Solid Earth*, *84*(B5), 2161–2168.

Dieterich, J. H. (1994). A constitutive law for rate of earthquake production and its application to earthquake clustering. *Journal of Geophysical Research: Solid Earth*, *99*(B2), 2601–2618.

Dong, P., Chen, R., Xia, K., Yao, W., Peng, Z., & Elsworth, D. (2022). Earthquake delay and rupture velocity in near-field dynamic triggering dictated by stress-controlled nucleation. *Seismological Research Letters*, *94*(2A), 913-924.

Dublanchet, P., Bernard, P., & Favreau, P. (2013). Creep modulation of Omori law generated by a Coulomb stress perturbation in a 3-D rate-and-state asperity model. *Journal of Geophysical Research: Solid Earth*, *118*(9), 4774–4793.

Dumbser, M., & Käser, M. (2006). An arbitrary high-order discontinuous Galerkin method for elastic waves on unstructured meshes—II. The three-dimensional isotropic case. *Geophysical Journal International*, *167*(1), 319–336.

Elkhoury, J. E., Brodsky, E. E., & Agnew, D. C. (2006). Seismic waves increase permeability. *Nature*, *441*(7097), 1135–1138.

Erickson, B. A., & Dunham, E. M. (2014). An efficient numerical method for earthquake cycles in heterogeneous media: Alternating subbasin and surface-rupturing events on faults crossing a sedimentary basin. *Journal of Geophysical Research: Solid Earth*, *119*(4), 3290–3316.

Farain, K., & Bonn, D. (2024). Perturbation-induced granular fluidization as a model for remote earthquake triggering. *Science Advances*, *10*(16), eadi7302.

Felzer, K. R., & Brodsky, E. E. (2005). Testing the stress shadow hypothesis. *Journal of Geophysical Research: Solid Earth*, *110*(B5).

Felzer, K. R., & Brodsky, E. E. (2006). Decay of aftershock density with distance indicates triggering by dynamic stress. *Nature*, *441*(7094), 735–738.

Freed, A. M. (2005). Earthquake triggering by static, dynamic, and postseismic stress transfer. *Annu. Rev. Earth Planet. Sci.*, *33*, 335–367.

Gabriel, A.-A., Garagash, D. I., Palgunadi, K. H., & Mai, P. M. (2024). Fault size–dependent fracture energy explains multiscale seismicity and cascading earthquakes. *Science*, *385*(6707), eadj9587.

Gabriel, A.-A., Kurapati, V., Niu, Z., Schliwa, N., Schneller, D., Ulrich, T., ... Bader, M. (2025). *SeisSol.* (v1.3.2) [Software]. Zenodo. doi: https://doi.org/10.5281/zenodo.15685917

Gabriel, A.-A., Ulrich, T., Marchandon, M., Biemiller, J., & Rekoske, J. (2023). 3D Dynamic Rupture Modeling of the 6 February 2023, Kahramanmaraş, Turkey M_w 7.8 and 7.7 Earthquake Doublet Using Early Observations. *The Seismic Record*, *3*(4), 342–356.

Galis, M., Ampuero, J. P., Mai, P. M., & Cappa, F. (2017). Induced seismicity provides insight into why earthquake ruptures stop. *Science advances*, *3*(12), eaap7528.

Gallovič, F. (2008). Heterogeneous Coulomb stress perturbation during earthquake cycles in a 3D rate-and-state fault model. *Geophysical research letters*, *35*(21).

Garagash, D. I., & Germanovich, L. N. (2012). Nucleation and arrest of dynamic slip on a pressurized fault. *Journal of Geophysical Research: Solid Earth*, *117*(B10).

Goldberg, D. E., Melgar, D., Sahakian, V., Thomas, A., Xu, X., Crowell, B., & Geng, J. (2020). Complex rupture of an immature fault zone: A simultaneous kinematic model of the 2019 Ridgecrest, CA earthquakes. *Geophysical Research Letters*, *47*(3), e2019GL086382.

Gomberg, J. (1996). Stress/strain changes and triggered seismicity following the M_w 7.3 Landers, California earthquake. *Journal of Geophysical Research: Solid Earth*, *101*(B1), 751–764.

Gomberg, J., Beeler, N., Blanpied, M., & Bodin, P. (1998). Earthquake triggering by transient and static deformations. *Journal of Geophysical Research: Solid Earth*, *103*(B10), 24411–24426.

Gomberg, J., Blanpied, M. L., & Beeler, N. (1997). Transient triggering of near and distant earthquakes. *Bulletin of the Seismological Society of America*, *87*(2), 294–309.

Gomberg, J., Reasenberg, P., Bodin, P. l., & Harris, R. (2001). Earthquake triggering by seismic waves following the Landers and Hector Mine earthquakes. *Nature*, *411*(6836), 462–466.

Guo, H., Brodsky, E. E., & Miyazawa, M. (2024). Triggering Intensity Changes over Time and Space as Measured by Continuous Waveforms in southern California. *ESS Open Archive eprints*, *867*, 172222568–86733850.

Hardebeck, J. L., & Harris, R. A. (2022). Earthquakes in the shadows: Why aftershocks occur at surprising locations. *The Seismic Record*, *2*(3), 207–216.

Harris, R. A., & Simpson, R. W. (1992). Changes in static stress on southern California faults after the 1992 Landers earthquake. *Nature*, *360*(6401), 251–254.

Harris, R. A., & Simpson, R. W. (1996). In the shadow of 1857-the effect of the great Ft. Tejon earthquake on subsequent earthquakes in southern California. *Geophysical Research Letters*, *23*(3), 229–232.

Harris, R. A., & Simpson, R. W. (1998). Suppression of large earthquakes by stress shadows: A comparison of Coulomb and rate-and-state failure. *Journal of Geophysical Research: Solid Earth*, *103*(B10), 24439–24451.

Hauksson, E., & Jones, L. M. (2020). Seismicity, stress state, and style of faulting of the Ridgecrest-Coso region from the 1930s to 2019: Seismotectonics of an evolving plate boundary segment. *Bulletin of the Seismological Society of America*, *110*(4), 1457–1473.

Heinecke, A., Breuer, A., Rettenberger, S., Bader, M., Gabriel, A.-A., Pelties, C., ... others (2014). Petascale high order dynamic rupture earthquake simulations on heterogeneous supercomputers. In *Sc'14: Proceedings of the international conference for high performance computing, networking, storage and analysis* (pp. 3–14).

Helmstetter, A., Sornette, D., & Grasso, J.-R. (2003). Mainshocks are aftershocks of conditional foreshocks: How do foreshock statistical properties emerge from aftershock laws. *Journal of Geophysical Research: Solid Earth*, *108*(B1).

Hill, D. P., & Prejean, S. (2015). 4.11 - Dynamic Triggering. In G. Schubert (Ed.), *Treatise on geophysics (second edition)* (Second Edition ed., p. 273-304). Oxford: Elsevier. doi: https://doi.org/10.1016/B978-0-444-53802-4.00078-6

Hill, D. P., Reasenberg, P., Michael, A., Arabaz, W., Beroza, G., Brumbaugh, D., ... others (1993). Seismicity remotely triggered by the magnitude 7.3 Landers, California, earthquake. *Science*, *260*(5114), 1617–1623.

Hirose, F., Miyaoka, K., Hayashimoto, N., Yamazaki, T., & Nakamura, M. (2011). Outline of the 2011 off the Pacific coast of Tohoku Earthquake (M_w 9.0) - Seismicity: foreshocks, mainshock, aftershocks, and induced activity -. *Earth, planets and space*, *63*, 513–518.

Hori, T., & Kaneda, Y. (2001). A simple explanation for the occurrence of the 1911 Morgan Hill earthquake in the stress shadow of the 1906 San Francisco earthquake. *Geophysical research letters*, *28*(11), 2261–2264.

Huang, H., Meng, L., Bürgmann, R., Wang, W., & Wang, K. (2020). Spatiotemporal foreshock evolution of the 2019 M 6.4 and M 7.1 Ridgecrest, California earthquakes. *Earth and Planetary Science Letters*, *551*, 116582.

Hudnut, K. W., Seeber, L., & Pacheco, J. (1989). Cross-fault triggering in the November 1987 Superstition Hills earthquake sequence, southern California. *Geophysical Research Letters*, *16*(2), 199–202.

Husen, S., Wiemer, S., & Smith, R. B. (2004). Remotely triggered seismicity in the Yellowstone National Park region by the 2002 M_w 7.9 Denali fault earthquake, Alaska. *Bulletin of the Seismological Society of America*, *94*(6B), S317–S331.

Ida, Y. (1972). Cohesive force across the tip of a longitudinal-shear crack and Griffith's specific surface energy. *Journal of Geophysical Research*, *77*(20), 3796–3805.

Inbal, A., Ziv, A., Lior, I., Nof, R. N., & Eisermann, A. S. (2023). Non-triggering and then triggering of a repeating aftershock sequence in the Dead Sea by the 2023 Kahramanmaraş Earthquake pair: Implications for the physics of remote delayed aftershocks. *Geophysical Research Letters*, *50*(18), e2023GL104908.

Jia, Z., Jin, Z., Marchandon, M., Ulrich, T., Gabriel, A.-A., Fan, W., ... others (2023). The complex dynamics of the 2023 Kahramanmaraş, Turkey, M_w 7.8-7.7 earthquake doublet. *Science*, *381*(6661), 985–990.

Jia, Z., Wang, X., & Zhan, Z. (2020). Multifault models of the 2019 Ridgecrest sequence highlight complementary slip and fault junction instability. *Geophysical Research Letters*, *47*(17), e2020GL089802.

Jin, Y., Dyaur, N., & Zheng, Y. (2021). Laboratory evidence of transient pressure surge in a fluid-filled fracture as a potential driver of remote dynamic

earthquake triggering. *The Seismic Record*, *1*(2), 66–74.

Jin, Z., & Fialko, Y. (2020). Finite slip models of the 2019 Ridgecrest earthquake sequence constrained by space geodetic data and aftershock locations. *Bulletin of the Seismological Society of America*, *110*(4), 1660–1679.

Jin, Z., Fialko, Y., Zubovich, A., & Schöne, T. (2022). Lithospheric deformation due to the 2015 M7.2 Sarez (Pamir) earthquake constrained by 5 years of space geodetic observations. *Journal of Geophysical Research: Solid Earth*, *127*, e2021JB022461.

Johnson, P. A., & Jia, X. (2005). Nonlinear dynamics, granular media and dynamic earthquake triggering. *Nature*, *437*(7060), 871–874.

Jones, L. M., & Molnar, P. (1979). Some characteristics of foreshocks and their possible relationship to earthquake prediction and premonitory slip on faults. *Journal of Geophysical Research: Solid Earth*, *84*(B7), 3596–3608.

Kaneko, Y., & Lapusta, N. (2008). Variability of earthquake nucleation in continuum models of rate-and-state faults and implications for aftershock rates. *Journal of Geophysical Research: Solid Earth*, *113*(B12).

Katakami, S., Kaneko, Y., Ito, Y., & Araki, E. (2020). Stress sensitivity of instantaneous dynamic triggering of shallow slow slip events. *Journal of Geophysical Research: Solid Earth*, *125*(6), e2019JB019178.

Kilb, D., Gomberg, J., & Bodin, P. (2000). Triggering of earthquake aftershocks by dynamic stresses. *Nature*, *408*(6812), 570–574.

King, G. C., Stein, R. S., & Lin, J. (1994). Static stress changes and the triggering of earthquakes. *Bulletin of the Seismological Society of America*, *84*(3), 935–953.

Kostka, F., & Gallovič, F. (2016). Static Coulomb stress load on a three-dimensional rate-and-state fault: Possible explanation of the anomalous delay of the 2004 Parkfield earthquake. *Journal of Geophysical Research: Solid Earth*, *121*(5), 3517–3533.

Krenz, L., Uphoff, C., Ulrich, T., Gabriel, A.-A., Abrahams, L. S., Dunham, E. M., & Bader, M. (2021). 3D acoustic-elastic coupling with gravity: the dynamics of the 2018 Palu, Sulawesi earthquake and tsunami. In *Proceedings of the international conference for high performance computing, networking, storage and analysis* (pp. 1–14).

Kroll, K. A., Richards-Dinger, K. B., Dieterich, J. H., & Cochran, E. S. (2017). Delayed seismicity rate changes controlled by static stress transfer. *Journal of Geophysical Research: Solid Earth*, *122*(10), 7951–7965.

Lapusta, N., Rice, J. R., Ben-Zion, Y., & Zheng, G. (2000). Elastodynamic analysis for slow tectonic loading with spontaneous rupture episodes on faults with rate-and state-dependent friction. *Journal of Geophysical Research: Solid Earth*, *105*(B10), 23765–23789.

Lee, E.-J., Chen, P., Jordan, T. H., Maechling, P. J., Denolle, M. A., & Beroza, G. C. (2014). Full-3-D tomography for crustal structure in southern California based on the scattering-integral and the adjoint-wavefield methods. *Journal of Geophysical Research: Solid Earth*, *119*(8), 6421–6451.

Li, D., & Gabriel, A.-A. (2024). Linking 3D long-term slow-slip cycle models with rupture dynamics: The nucleation of the 2014 M_w 7.3 Guerrero, Mexico earthquake. *AGU Advances*, *5*(2), e2023AV000979.

Li, S., Chen, G., Tao, T., He, P., Ding, K., Zou, R., ... Wang, Q. (2020). The 2019 Mw 6.4 and Mw 7.1 Ridgecrest earthquake sequence in eastern California: Rupture on a conjugate fault structure revealed by GPS and InSAR measurements. *Geophysical Journal International*, *221*(3), 1651–1666.

Linker, M., & Dieterich, J. H. (1992). Effects of variable normal stress on rock friction: Observations and constitutive equations. *Journal of Geophysical Research: Solid Earth*, *97*(B4), 4923–4940.

Liu, D., Duan, B., & Luo, B. (2020). EQsimu: a 3-D finite element dynamic earth-

quake simulator for multicycle dynamics of geometrically complex faults governed by rate-and state-dependent friction. *Geophysical Journal International*, *220*(1), 598–609.

Luo, Y., & Liu, Z. (2019). Slow-slip recurrent pattern changes: Perturbation responding and possible scenarios of precursor toward a megathrust earthquake. *Geochemistry, Geophysics, Geosystems*, *20*(2), 852–871.

Magen, Y., Ziv, A., Inbal, A., Baer, G., & Hollingsworth, J. (2020). Fault rerupture during the July 2019 Ridgecrest earthquake pair from joint slip inversion of InSAR, optical imagery, and GPS. *Bulletin of the Seismological Society of America*, *110*(4), 1627–1643.

Marsan, D. (2006). Can coseismic stress variability suppress seismicity shadows? Insights from a rate-and-state friction model. *Journal of Geophysical Research: Solid Earth*, *111*(B6).

Meng, H., & Fan, W. (2021). Immediate foreshocks indicating cascading rupture developments for 527 M 0.9 to 5.4 Ridgecrest earthquakes. *Geophysical Research Letters*, *48*(19), e2021GL095704.

Mitchell, E., Fialko, Y., & Brown, K. (2015). Frictional properties of gabbro at conditions corresponding to slow slip events in subduction zones. *Geochemistry, Geophysics, Geosystems*, *16*(11), 4006–4020.

Mosconi, F., Tinti, E., Casarotti, E., Gabriel, A.-A., Rinaldi, A. P., Dal Zilio, L., & Cocco, M. (2025). Modeling the 3D dynamic rupture of microearthquakes induced by fluid injection. *Journal of Geophysical Research: Solid Earth*, *130*(3), e2024JB029621.

Oeser, J., Bunge, H.-P., & Mohr, M. (2006). Cluster design in the earth sciences tethys. In *International conference on high performance computing and communications* (pp. 31–40).

Palmer, A. C., & Rice, J. R. (1973). The growth of slip surfaces in the progressive failure of over-consolidated clay. *Proceedings of the Royal Society of London. A. Mathematical and Physical Sciences*, *332*(1591), 527–548.

Parsons, T. (2005). A hypothesis for delayed dynamic earthquake triggering. *Geophysical Research Letters*, *32*(4).

Parsons, T., & Dreger, D. S. (2000). Static-stress impact of the 1992 Landers earthquake sequence on nucleation and slip at the site of the 1999 M= 7.1 Hector Mine earthquake, southern California. *Geophysical research letters*, *27*(13), 1949–1952.

Pelties, C., Gabriel, A.-A., & Ampuero, J.-P. (2014). Verification of an ADER-DG method for complex dynamic rupture problems. *Geoscientific Model Development*, *7*(3), 847–866.

Perfettini, H., Schmittbuhl, J., & Cochard, A. (2003a). Shear and normal load perturbations on a two-dimensional continuous fault: 1. Static triggering. *Journal of Geophysical Research: Solid Earth*, *108*(B9).

Perfettini, H., Schmittbuhl, J., & Cochard, A. (2003b). Shear and normal load perturbations on a two-dimensional continuous fault: 2. Dynamic triggering. *Journal of Geophysical Research: Solid Earth*, *108*(B9).

Perfettini, H., Schmittbuhl, J., Rice, J. R., & Cocco, M. (2001). Frictional response induced by time-dependent fluctuations of the normal loading. *Journal of Geophysical Research: Solid Earth*, *106*(B7), 13455–13472.

Pignalberi, F., Giorgetti, C., Noël, C., Marone, C., Collettini, C., & Scuderi, M. M. (2024). The effect of normal stress oscillations on fault slip behavior near the stability transition from stable to unstable motion. *Journal of Geophysical Research: Solid Earth*, *129*(2), e2023JB027470.

Pranger, C. C. (2020). *Unstable physical processes operating on self-governing fault systems, improved modeling methodology* (Unpublished doctoral dissertation). ETH Zurich.

Ramos, M. D., Thakur, P., Huang, Y., Harris, R. A., & Ryan, K. J. (2022). Working

with dynamic earthquake rupture models: A practical guide. *Seismological Society of America*, *93*(4), 2096–2110.

Reasenberg, P. A. (1999). Foreshock occurrence before large earthquakes. *Journal of Geophysical Research: Solid Earth*, *104*(B3), 4755–4768.

Reasenberg, P. A., & Simpson, R. W. (1992). Response of regional seismicity to the static stress change produced by the Loma Prieta earthquake. *Science*, *255*(5052), 1687–1690.

Rice, J. R., & Tse, S. T. (1986). Dynamic motion of a single degree of freedom system following a rate and state dependent friction law. *Journal of Geophysical Research: Solid Earth*, *91*(B1), 521–530.

Richardson, E., & Marone, C. (1999). Effects of normal stress vibrations on frictional healing. *Journal of Geophysical Research: Solid Earth*, *104*(B12), 28859–28878.

Ross, Z. E., Idini, B., Jia, Z., Stephenson, O. L., Zhong, M., Wang, X., ... others (2019). Hierarchical interlocked orthogonal faulting in the 2019 Ridgecrest earthquake sequence. *Science*, *366*(6463), 346–351.

Ruina, A. (1983). Slip instability and state variable friction laws. *Journal of Geophysical Research: Solid Earth*, *88*(B12), 10359–10370.

SCEDC. (2013). *Southern California Earthquake Data Center.* Caltech. [Dataset]. Retrieved from `http://scedc.caltech.edu` doi: 10.7909/C3WD3XH1

Shelly, D. R. (2020). A high-resolution seismic catalog for the initial 2019 Ridgecrest earthquake sequence: Foreshocks, aftershocks, and faulting complexity. *Seismological Research Letters*, *91*(4), 1971–1978.

Shelly, D. R., Peng, Z., Hill, D. P., & Aiken, C. (2011). Triggered creep as a possible mechanism for delayed dynamic triggering of tremor and earthquakes. *Nature Geoscience*, *4*(6), 384–388.

Small, P. E., Gill, D., Maechling, P. J., Taborda, R., Callaghan, S., Jordan, T. H., ... Goulet, C. (2017). The SCEC unified community velocity model software framework. *Seismological Research Letters*, *88*(6), 1539–1552.

Small, P. E., Maechling, P. J., & Su, M.-H. (2022). *The Unified Community Velocity Model (UCVM).* (Version 22.7.0). [Dataset]. Zenodo. doi: https://doi.org/10.5281/zenodo.7033687

Stein, R. S. (1999). The role of stress transfer in earthquake occurrence. *Nature*, *402*(6762), 605–609.

Taufiqurrahman, T., Gabriel, A.-A., Li, D., Ulrich, T., Li, B., Carena, S., ... Gallovič, F. (2023). Dynamics, interactions and delays of the 2019 Ridgecrest rupture sequence. *Nature*, *618*(7964), 308–315.

Thakur, P., Huang, Y., & Kaneko, Y. (2020). Effects of low-velocity fault damage zones on long-term earthquake behaviors on mature strike-slip faults. *Journal of Geophysical Research: Solid Earth*, *125*(8), e2020JB019587.

Toda, S., Stein, R. S., Beroza, G. C., & Marsan, D. (2012). Aftershocks halted by static stress shadows. *Nature Geoscience*, *5*(6), 410–413.

Tymofyeyeva, E., Fialko, Y., Jiang, J., Xu, X., Sandwell, D., Bilham, R., ... others (2019). Slow slip event on the Southern San Andreas fault triggered by the 2017 M_w 8.2 Chiapas (Mexico) earthquake. *Journal of Geophysical Research: Solid Earth*, *124*(9), 9956–9975.

Ulrich, T., Gabriel, A.-A., Ampuero, J.-P., & Xu, W. (2019). Dynamic viability of the 2016 M_w 7.8 Kaikōura earthquake cascade on weak crustal faults. *Nature communications*, *10*(1), 1213.

Uphoff, C., May, D. A., & Gabriel, A.-A. (2022). *A discontinuous Galerkin method for sequences of earthquakes and aseismic slip on multiple faults using unstructured curvilinear grids. Geophysical Journal International.* (Version 1.0) [Software]. Zenodo. doi: https://doi.org/10.5281/zenodo.5796104

Uphoff, C., May, D. A., & Gabriel, A.-A. (2023). A discontinuous Galerkin method for sequences of earthquakes and aseismic slip on multiple faults using unstruc-

tured curvilinear grids. *Geophysical Journal International*, *233*(1), 586–626.

Uphoff, C., Rettenberger, S., Bader, M., Madden, E. H., Ulrich, T., Wollherr, S., & Gabriel, A.-A. (2017). Extreme scale multi-physics simulations of the tsunamigenic 2004 Sumatra megathrust earthquake. In *Proceedings of the international conference for high performance computing, networking, storage and analysis* (pp. 1–16).

USGS. (2017). *Advanced National Seismic System (ANSS) Comprehensive Catalog.* U.S. Geological Survey. [Dataset]. Retrieved from `http://earthquake.usgs.gov/earthquakes/search/` doi: 10.5066/F7MS3QZH

USGS. (2020). *Quaternary Fault and Fold Database for the Nation.* [Dataset]. Retrieved from `https://www.usgs.gov/programs/earthquake-hazards/faults` doi: https://doi.org/10.5066/P9BCVRCK

van der Elst, N. J., & Brodsky, E. E. (2010). Connecting near-field and far-field earthquake triggering to dynamic strain. *Journal of Geophysical Research: Solid Earth*, *115*(B7).

van der Elst, N. J., & Savage, H. M. (2015). Frequency dependence of delayed and instantaneous triggering on laboratory and simulated faults governed by rate-state friction. *Journal of Geophysical Research: Solid Earth*, *120*(5), 3406–3429.

van der Elst, N. J., & Shaw, B. E. (2015). Larger aftershocks happen farther away: Nonseparability of magnitude and spatial distributions of aftershocks. *Geophysical Research Letters*, *42*(14), 5771–5778.

Wang, K., Dreger, D. S., Tinti, E., Bürgmann, R., & Taira, T. (2020). Rupture process of the 2019 Ridgecrest, California M w 6.4 foreshock and M w 7.1 earthquake constrained by seismic and geodetic data. *Bulletin of the Seismological Society of America*, *110*(4), 1603–1626.

Wang, K., & Fialko, Y. (2014). Space geodetic observations and models of postseismic deformation due to the 2005 M7.6 Kashmir (Pakistan) earthquake. *Journal of Geophysical Research: Solid Earth*, *119*(9), 7306–7318.

Wei, M., Kaneko, Y., Shi, P., & Liu, Y. (2018). Numerical modeling of dynamically triggered shallow slow slip events in New Zealand by the 2016 M_w 7.8 Kaikoura earthquake. *Geophysical Research Letters*, *45*(10), 4764–4772.

Wollherr, S., Gabriel, A.-A., & Uphoff, C. (2018). Off-fault plasticity in three-dimensional dynamic rupture simulations using a modal Discontinuous Galerkin method on unstructured meshes: implementation, verification and application. *Geophysical Journal International*, *214*(3), 1556–1584.

Yoshida, S., Maeda, T., & Kato, N. (2020). Earthquake triggering model based on normal-stress-dependent Nagata law: application to the 2016 Mie offshore earthquake. *Earth, Planets and Space*, *72*, 1–13.

Yue, H., Sun, J., Wang, M., Shen, Z., Li, M., Xue, L., ... Lay, T. (2021). The 2019 Ridgecrest, California earthquake sequence: Evolution of seismic and aseismic slip on an orthogonal fault system. *Earth and Planetary Science Letters*, *570*, 117066.

Yun, J., Gabriel, A.-A., May, D. A., & Fialko, Y. (2025a). Effects of Stress and Friction Heterogeneity on Spatiotemporal Complexity of Seismic and Aseismic Slip on Strike-Slip Faults. *Journal of Geophysical Research: Solid Earth*.

Yun, J., Gabriel, A.-A., May, D. A., & Fialko, Y. (2025b). *Supplementary material for "Controls of Dynamic and Static Stress Changes and Aseismic Slip on Delayed Earthquake Triggering: Application to the 2019 Ridgecrest Earthquake Sequence.* (Version v1) [Dataset]. Zenodo. doi: https://doi.org/10.5281/zenodo.14716334

Zhu, W., Allison, K. L., Dunham, E. M., & Yang, Y. (2020). Fault valving and pore pressure evolution in simulations of earthquake sequences and aseismic slip. *Nature communications*, *11*(1), 4833.

Supporting Information for "Controls of Dynamic and Static Stress Changes and Aseismic Slip on Delayed Earthquake Triggering: Application to the 2019 Ridgecrest Earthquake Sequence"

Jeena Yun[1], Alice-Agnes Gabriel[1,2], Dave A. May[1], and Yuri Fialko[1]

[1]Scripps Institution of Oceanography, University of California San Diego, La Jolla, CA, USA

[2]Department of Earth and Environmental Sciences, Ludwig-Maximilians Universität München, Munich, Germany

Contents of this file

Text S1. Comparison of synthetic and observed waveforms and analysis of the sensitivity of the spatiotemporal evolution of ΔCFS to the assumed fault geometry

To validate our models with observations, we compare synthetic seismograms with near-field waveforms recorded at stations CI.WRC2, CI.TOW2, and PB.B918 (Fig. S6). Slow initiation models show a closer fit to the observed waveforms than fast initiation models, while vertical and dipping foreshock fault models perform similarly. While the normalized waveforms agree satisfactorily, the absolute amplitude of the synthetic waveforms deviates from the observed ones by a factor ranging from 0.7 to 7.8. This mismatch is possibly due to missing smaller-scale heterogeneity in fault geometry, friction, initial stress, and velocity model (Huang, 2021; Imperatori & Mai, 2013; Taufiqurrahman et al., 2022), or omitting attenuation and off-fault plasticity (Kaneko & Fialko, 2011; Okubo et al., 2019) in our simulations. Although one-to-one waveform fitting with forward dynamic rupture simulations is not the primary goal of this study, these comparisons support the use of slow initiation scenarios to capture the first-order features of stress changes induced by the M_w 5.4 foreshock.

Varying the mainshock fault strike systematically affects the amplitude of the peak dynamic ΔCFS and the static ΔCFS, while varying the foreshock fault dip affects the seismic radiation, altering the arrival time, depth, and amplitude. More northerly strike angles systematically decrease the amplitude of the peak dynamic ΔCFS and the static ΔCFS (Fig. S5). Although the foreshock fault dip does not significantly affect the peak dynamic ΔCFS values, the dipping foreshock fault produces a stronger contrast between the positive and negative static ΔCFS values (Figs. S5c-d). The vertical foreshock fault

produces near-symmetric wave propagation with respect to a depth of ∼7 km, whereas the dipping foreshock fault shows asymmetric propagation (top vs. bottom rows of Fig. S4). This apparent asymmetry is caused by the asymmetric arrival of the strong dynamic ΔCFS pulse due to the rotation of the radiation field in the dipping foreshock fault models, although the actual rupture speed is similar for various depths. The rotation of the radiation field also makes the depth of the peak dynamic ΔCFS smaller, except for the 350° strike (Fig. S5b).

Text S2. Four Additional Reference SEAS Models

Figure S15 presents four reference SEAS models analyzed in Section 4.3 of the main text. The model in Figure S15a shares the same input parameters as the A2 reference model, but has a lower loading velocity $V_{\mathrm{pl}} = 3.2 \times 10^{-11}$ m/s. While the slip pattern remains similar to that of model A2, the mainshock recurrence interval increases from ∼76 yr in model A2 to ∼1915 yr in this low V_{pl} model. The model in Figure S15b incorporates fractal heterogeneities with shorter minimum (30 m; on the order of the critical nucleation size) and longer maximum (10 km; on the order of the seismogenic zone width) limiting wavelengths than those used in model A2 (minimum 500 m and maximum 2.5 km). This model is characterized by clustered seismicity at depths of 2 km, 7 km, and 10 km, corresponding to transitions between VS and VW behavior. Figures S15c and S15d show models N3R1D1 and N3R2D1, respectively, which are introduced in YGMF1 (see their Section 3.2, Figure 6). Both models adopt fractal heterogeneities with limiting wavelengths similar to model A2, but with a lower power-law exponent of the fractal distributions (i.e., a lower Hurst exponent), leading to increased short-wavelength roughness. Model N3R1D1 produces similar foreshock-mainshock sequences as model A2,

but its sequences consistently nucleate at the base of the seismogenic zone and migrate upward. Model N3R2D1, which uses a larger variation in $(a - b)$ amplitude compared to model N3R1D1, generates both shallow and deep slow slip events.

References

Dieterich, J. H. (1994). A constitutive law for rate of earthquake production and its application to earthquake clustering. *Journal of Geophysical Research: Solid Earth*, *99*(B2), 2601–2618.

Huang, Y. (2021). Smooth crustal velocity models cause a depletion of high-frequency ground motions on soil in 2D dynamic rupture simulations. *Bulletin of the Seismological Society of America*, *111*(4), 2057–2070.

Imperatori, W., & Mai, P. M. (2013). Broad-band near-field ground motion simulations in 3-dimensional scattering media. *Geophysical journal international*, *192*(2), 725–744.

Kaneko, Y., & Fialko, Y. (2011). Shallow slip deficit due to large strike-slip earthquakes in dynamic rupture simulations with elasto-plastic off-fault response. *Geophysical Journal International*, *186*(3), 1389–1403.

Okubo, K., Bhat, H. S., Rougier, E., Marty, S., Schubnel, A., Lei, Z., ... Klinger, Y. (2019). Dynamics, radiation, and overall energy budget of earthquake rupture with coseismic off-fault damage. *Journal of Geophysical Research: Solid Earth*, *124*(11), 11771–11801.

SCEDC. (2013). *Southern California Earthquake Data Center.* Caltech. [Dataset]. Retrieved from `http://scedc.caltech.edu` doi: 10.7909/C3WD3XH1

Taufiqurrahman, T., Gabriel, A.-A., Ulrich, T., Valentova, L., & Gallovič, F. (2022). Broadband dynamic rupture modeling with fractal fault roughness, frictional heterogeneity, viscoelasticity and topography: The 2016 Mw 6.2 Amatrice, Italy earthquake. *Geophysical Research Letters*, *49*(22), e2022GL098872.

Table S1. Parameters for the 3D dynamic rupture simulation using *SeisSol*. VFI: vertical foreshock fault, fast initiation; VSI: vertical foreshock fault, slow initiation; DFI: dipping foreshock fault, fast initiation; DSI: dipping foreshock fault, slow initiation.

Symbol	Parameter	Value			
		VFI	VSI	DFI	DSI
D_{LSW}	Critical slip-weakening distance	0.1 m	0.25 m	0.1 m	0.25 m
C_0	Frictional cohesion	0.2 MPa			
f_d	Dynamic friction coefficient				
	On nucleation patch	0.3743	0.3343	0.3328	0.2735
	On foreshock fault	0.471	0.431	0.4295	0.3702
	On mainshock fault	1000			
f_s	Static friction coefficient				
	On nucleation patch	$0.4433 - 0.4869$			
	On foreshock fault	$0.5841 - 0.7$			
	On mainshock fault	1000			
$\boldsymbol{\sigma}$	Initial stress tensor				
	Normal components ($\boldsymbol{\sigma}_{xx}$, $\boldsymbol{\sigma}_{yy}$, $\boldsymbol{\sigma}_{zz}$)	120 MPa			
	Along-strike shear component ($\boldsymbol{\sigma}_{xy}$)	70 MPa			
	Along-dip shear components ($\boldsymbol{\sigma}_{yz}$, $\boldsymbol{\sigma}_{xz}$)	0 MPa			

Table S2. Parameters used in the SEAS models using *Tandem*. Parameters a, D_{RS}, and σ_n show their average value, as these parameters include fractal heterogeneity. A2: 'A'ging law model with $\overline{D_{RS}} = 2$ mm, S10: 'S'lip law model with $\overline{D_{RS}} = 10$ mm, A10: 'A'ging law model with $\overline{D_{RS}} = 10$ mm.

Symbol	Parameter	Value
$\overline{a}$	Rate-and-state parameter, direct effect	Variable (see Fig. S1c)
b	Rate-and-state parameter, evolution effect	0.019
$\overline{D_{RS}}$	Characteristic state evolution distance	2 mm (A2) 10 mm (S10 & A10)
f_0	Reference coefficient of friction	0.6
V_0	Reference slip rate	10^{-6} m/s
V_{init}	Initial slip rate	10^{-9} m/s
V_{pl}	Plate loading rate	10^{-9} m/s
$\overline{\sigma_n}$	Background effective normal stress	50 MPa (see Fig. S1b)
τ^0	Background shear stress	10 - 30 MPa
μ	Bulk shear modulus	20 GPa
ν	Poisson's ratio	0.25
W	Seismogenic zone width*	∼10 km
L_f	Fault length	24 km

* May slightly vary due to fractal heterogeneity (see Fig. S1).

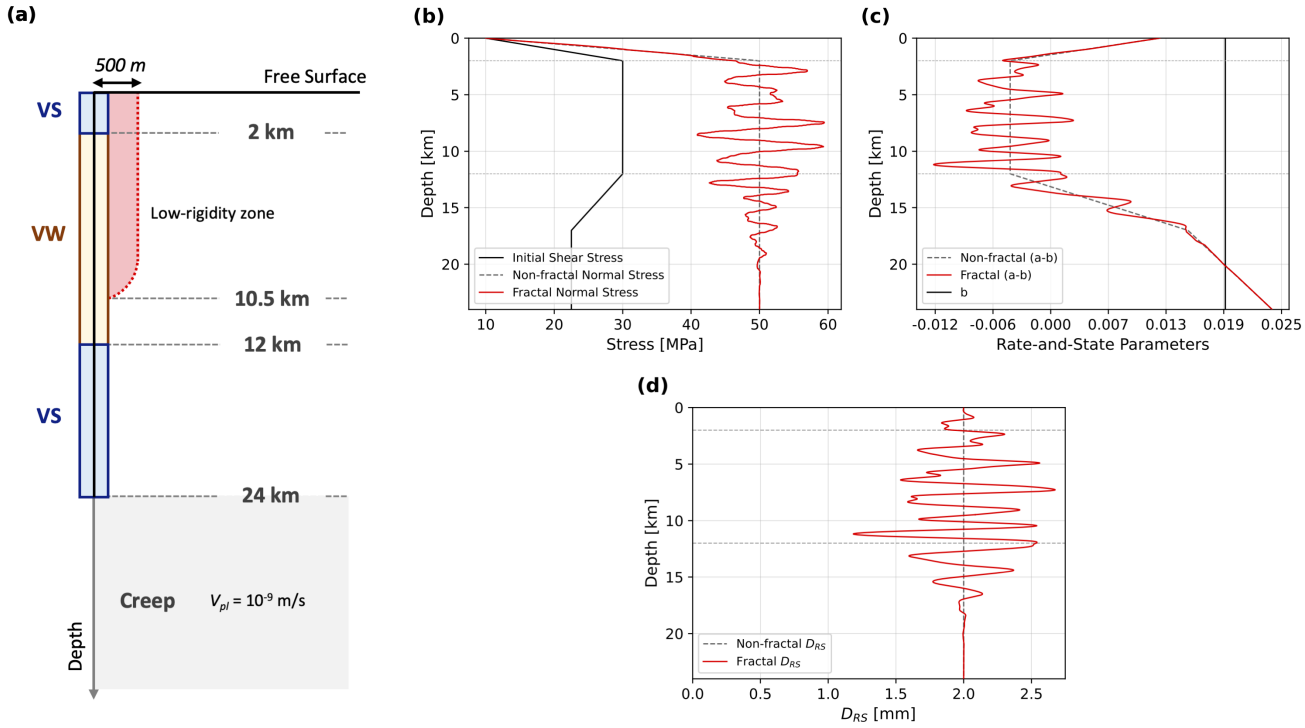

Figure S1. (a) Sketch of the model geometry for the SEAS simulations using *Tandem*. The rate-and-state fault (black vertical line) includes a central velocity-weakening zone (yellow) surrounded by shallow and deep velocity-strengthening zones (blue). The bottom creep zone governed by the constant loading rate (V_{pl}) is shaded in grey. The red-shaded area indicates the spatial extent of a low-rigidity fault zone. As the model represents a perfectly symmetric vertical strike-slip fault, we model only one side of the domain. (b-d) Self-affine fractal distributions of (b) effective normal stress, (c) rate-and-state parameters, and (d) characteristic state evolution distance, that parameterize the aging law reference model (A2; see Section 2.2 of the main text). The fractal distributions of all three parameters share the same limiting wavelengths of $\lambda_{min} = 500$ m and $\lambda_{max} = 2.5$ km.

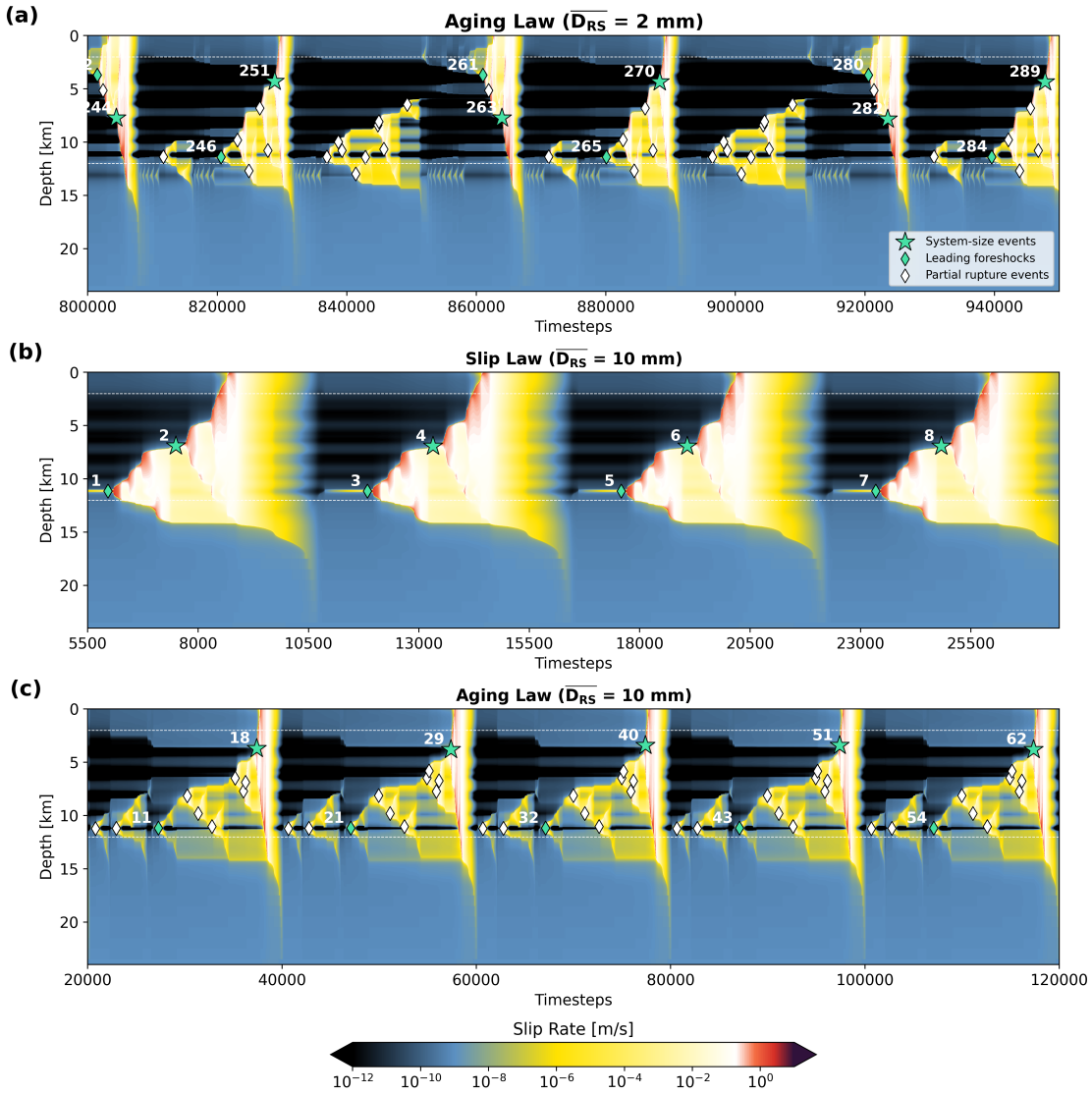

Figure S2. Spatiotemporal evolution of slip rate of reference SEAS models used in this study. (a) Reference aging law SEAS model (A2), showing the period between 2317 yr and 2681 yr of simulation time. (b) Reference slip law SEAS model (S10) and (c) the equivalent aging law model (A10). See Section 2.2 of the main text for detailed model descriptions. Event numbering starts from a non-zero value since we only show the spun-up phase of the models, i.e., after 200 yr of simulation time. Green stars, green diamonds, and white diamonds indicate the hypocenter locations of system-size earthquakes, leading foreshocks, and partial rupture events, respectively.

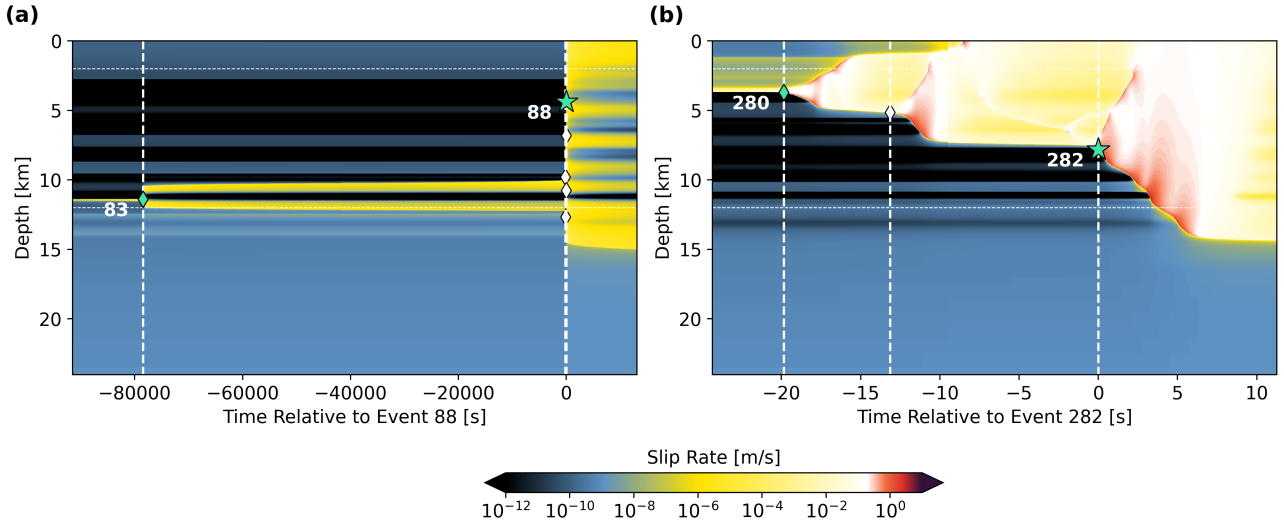

Figure S3. Examples of temporally clustered foreshock sequences in the aging law reference model (A2) with durations of (a) ∼1 day and (b) ∼20 seconds. The recurrence interval of mainshocks in this model is ∼76 yr.

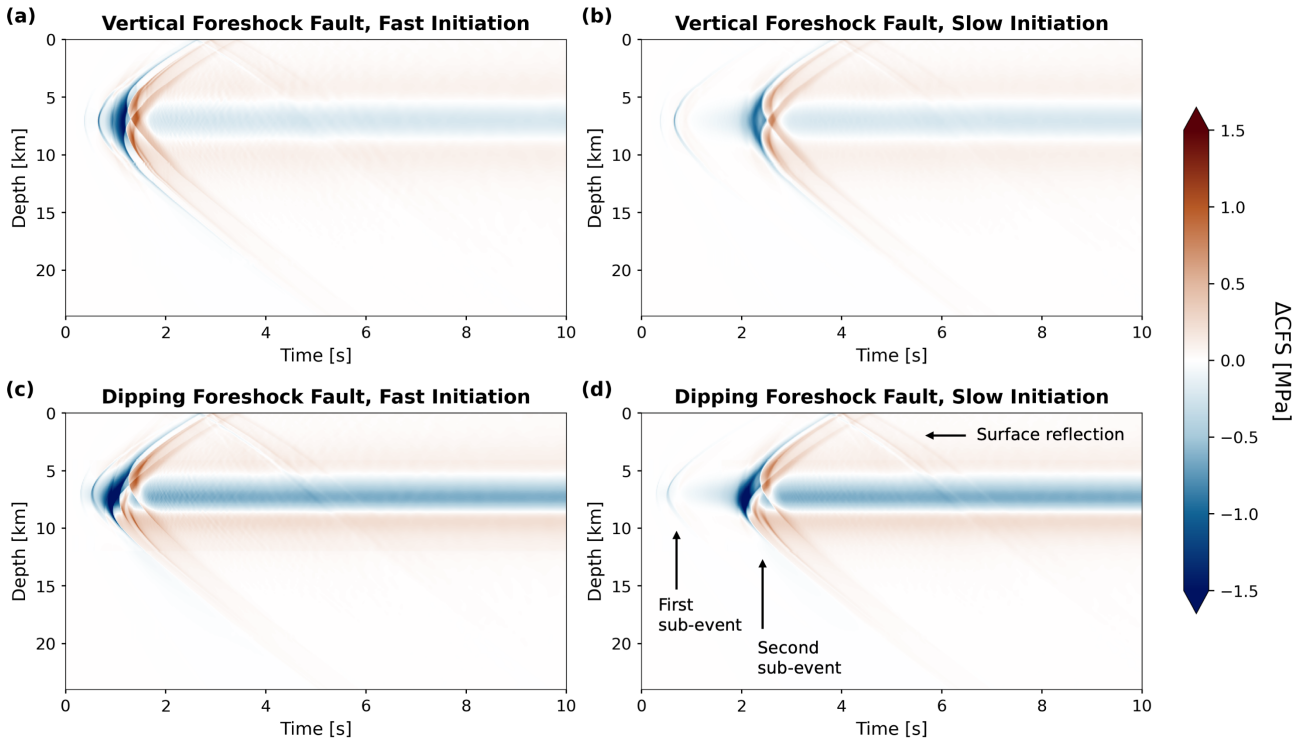

Figure S4. Spatiotemporal evolution of ΔCFS along the mainshock fault in 3D dynamic rupture models for (a) VFI, (b) VSI, (c) DFI, and (d) DSI models. All four models assume a mainshock fault strike of 340°. (VFI: vertical foreshock fault, fast initiation; VSI: vertical foreshock fault, slow initiation; DFI: dipping foreshock fault, fast initiation; DSI: dipping foreshock fault, slow initiation.)

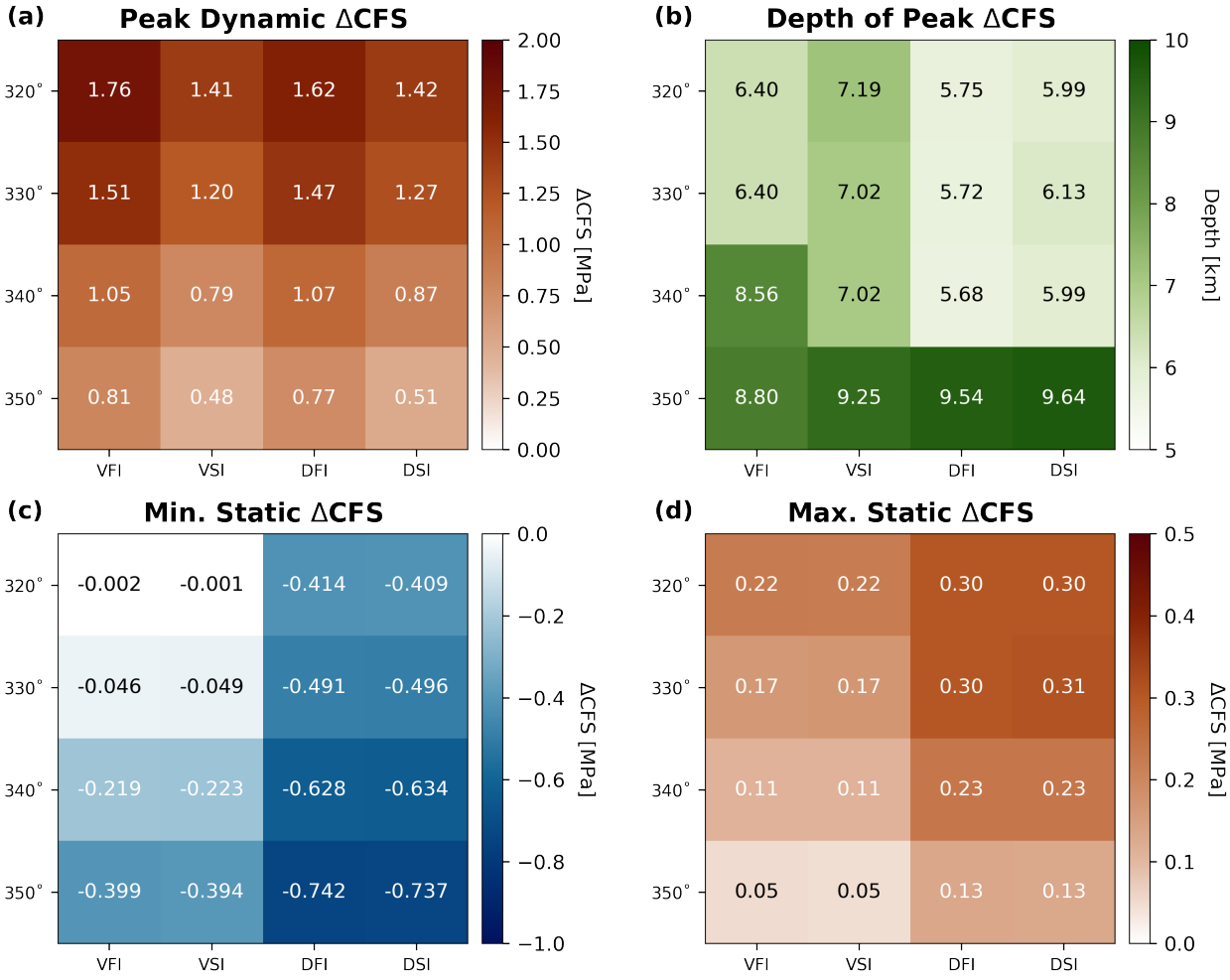

Figure S5. Summary of key values obtained from all 3D dynamic rupture models: (a) peak dynamic ΔCFS , (b) depth corresponding to the peak dynamic ΔCFS , (c) minimum static ΔCFS , and (d) maximum static ΔCFS . (VFI: vertical foreshock fault, fast initiation; VSI: vertical foreshock fault, slow initiation; DFI: dipping foreshock fault, fast initiation; DSI: dipping foreshock fault, slow initiation.)

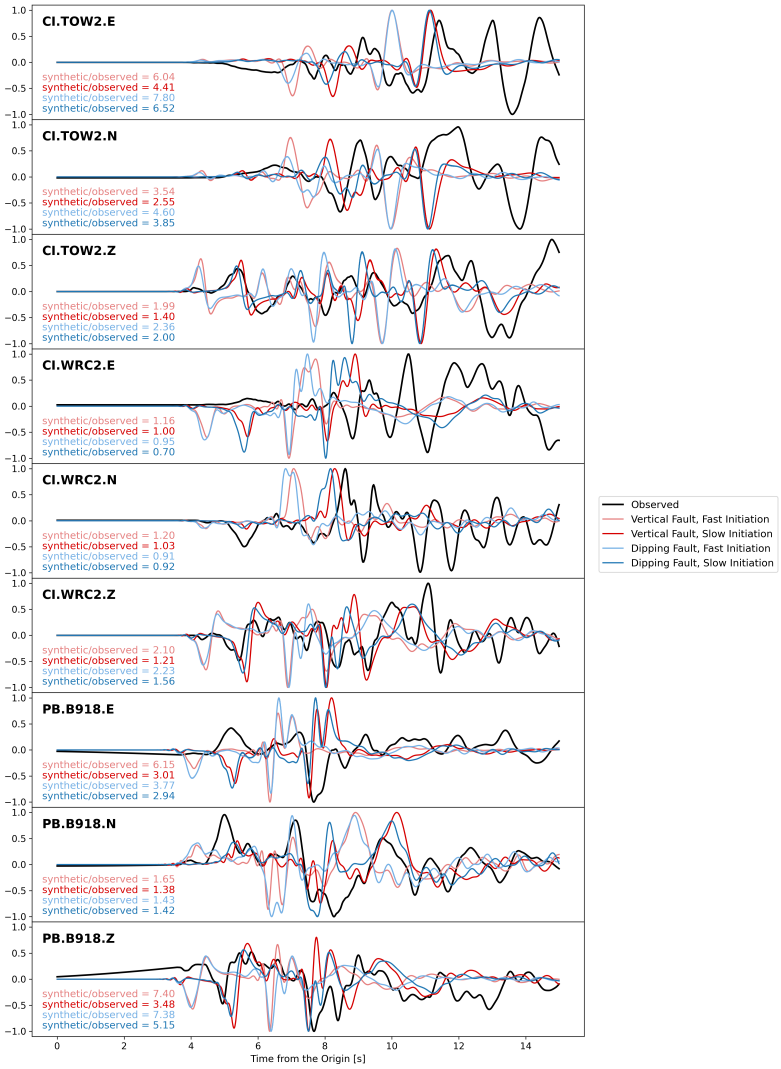

Figure S6. Comparison of synthetic seismograms from M_w 5.4 foreshock dynamic rupture models (colored lines) with observed waveforms (black lines; SCEDC, 2013) at three near-field stations: CI.WRC2, CI.TOW2, and PB.B918 (see triangle markers in Fig. 1 of the main text). Synthetic waveforms from all four model categories are shown: (1) vertical foreshock fault, fast initiation (pink lines); (2) vertical foreshock fault, slow initiation (red lines); (3) dipping foreshock fault, fast initiation (light blue lines); and (4) dipping foreshock fault, slow initiation (blue lines). Observed waveforms are bandpass filtered between 0.005 - 1 Hz. All waveforms are normalized in amplitude for visual comparison. The peak amplitude ratio (synthetic/observed) is indicated in each panel.

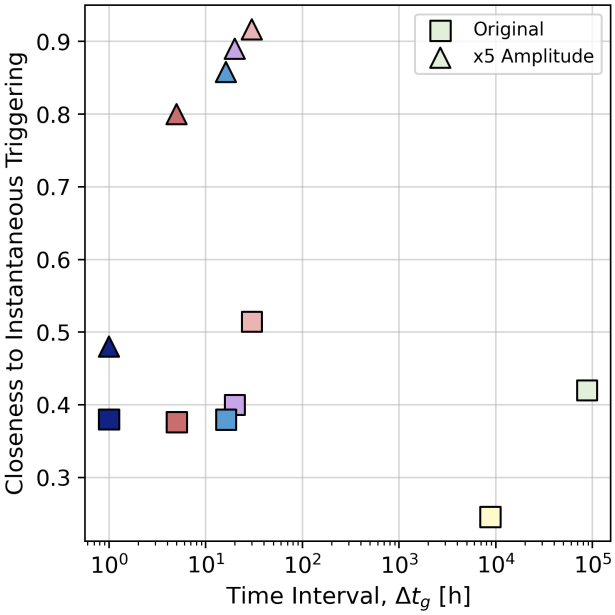

Figure S7. Closeness to instantaneous triggering (see Section 3.2 of the main text) for different perturbation timings (Δt_g). The squares represent the same SEAS simulations shown in Figure 5 of the main text while the triangles represent the SEAS simulations perturbing the same target event with 5-times amplified stress perturbation. The color scheme is identical to that in Figure 5 of the main text.)

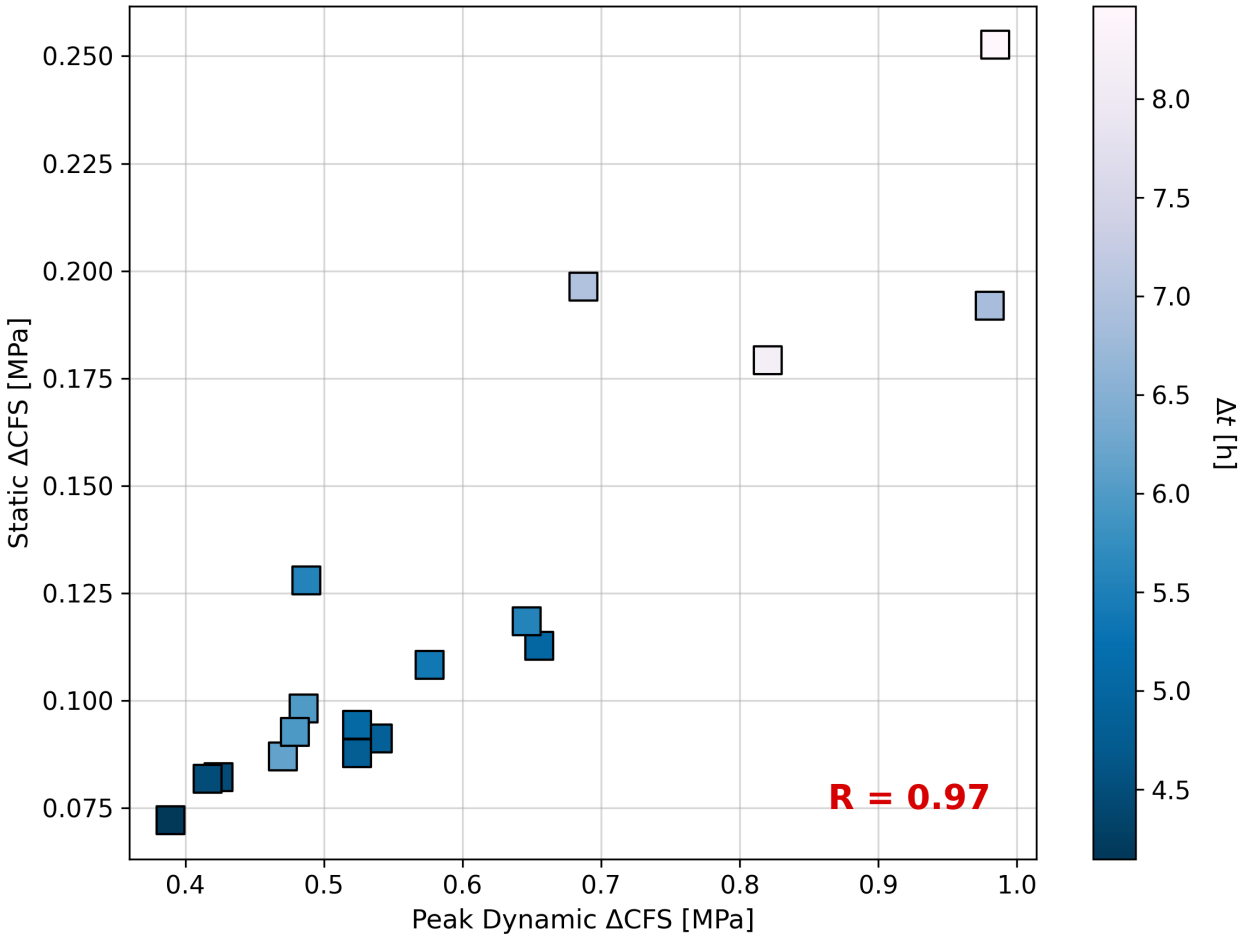

Figure S8. Correlation between peak dynamic ΔCFS and static ΔCFS obtained from all explored cases with the aging law reference model. The ΔCFS values are measured at a depth corresponding to the maximum aseismic slip during the perturbation period in each simulation (i.e., z_{max}). The Pearson correlation coefficient R is shown in the bottom right corner.

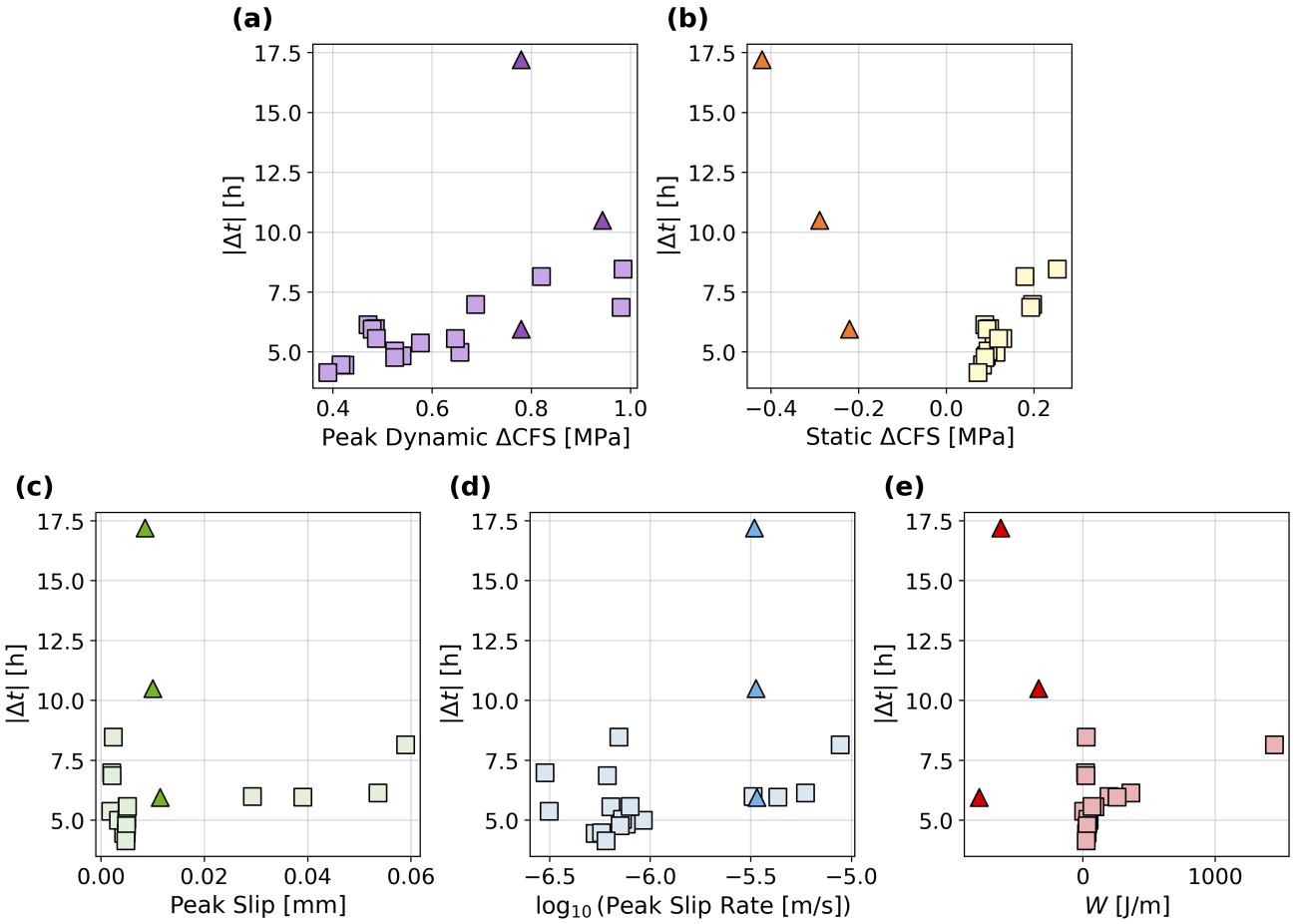

Figure S9. Same as Figure 4 of the main text (squares), but including clock delay models (triangles). For clarity, the absolute value of the mainshock clock change ($|\Delta t|$) is shown on the y-axis. A clear distinction between the clock advance models (squares) and the clock delay models (triangles) is observed in static ΔCFS (panel b) and work per distance, W (panel e).

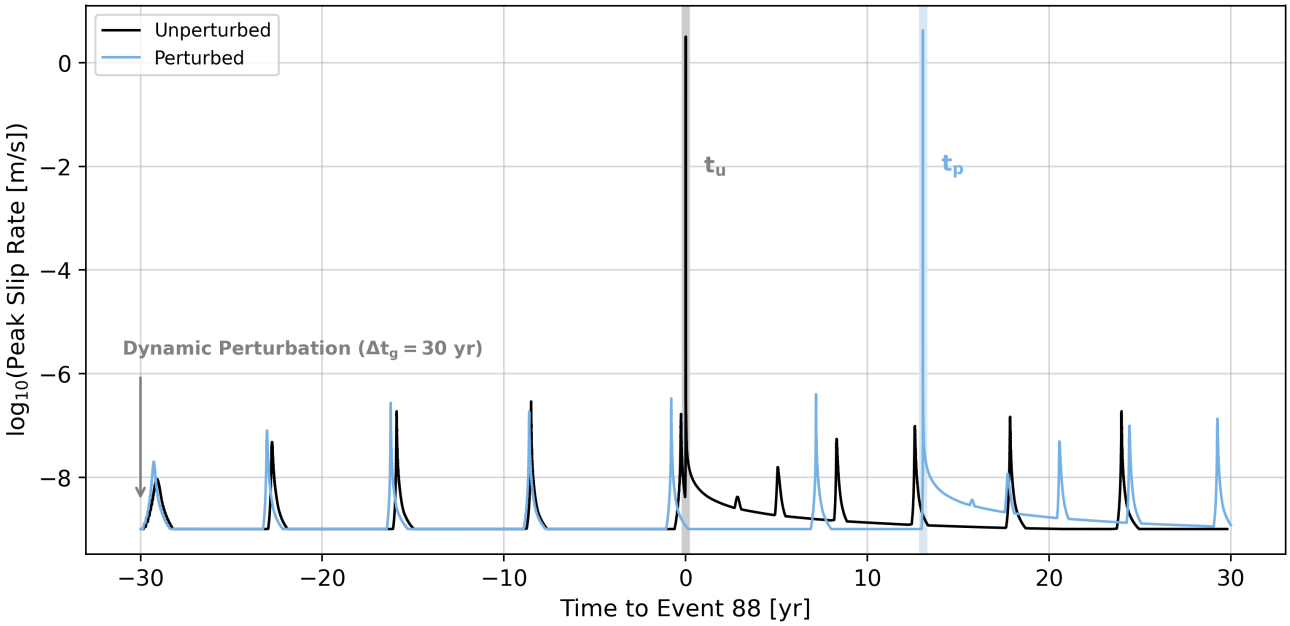

Figure S10. Peak slip rate of the unperturbed model (black) and perturbed model (blue) with $\Delta t_g = 30$ yr (grey arrow), showing ∼13 yr delay of the mainshock. The example simulation shown here is identical to that in Figure 5 of the main text.

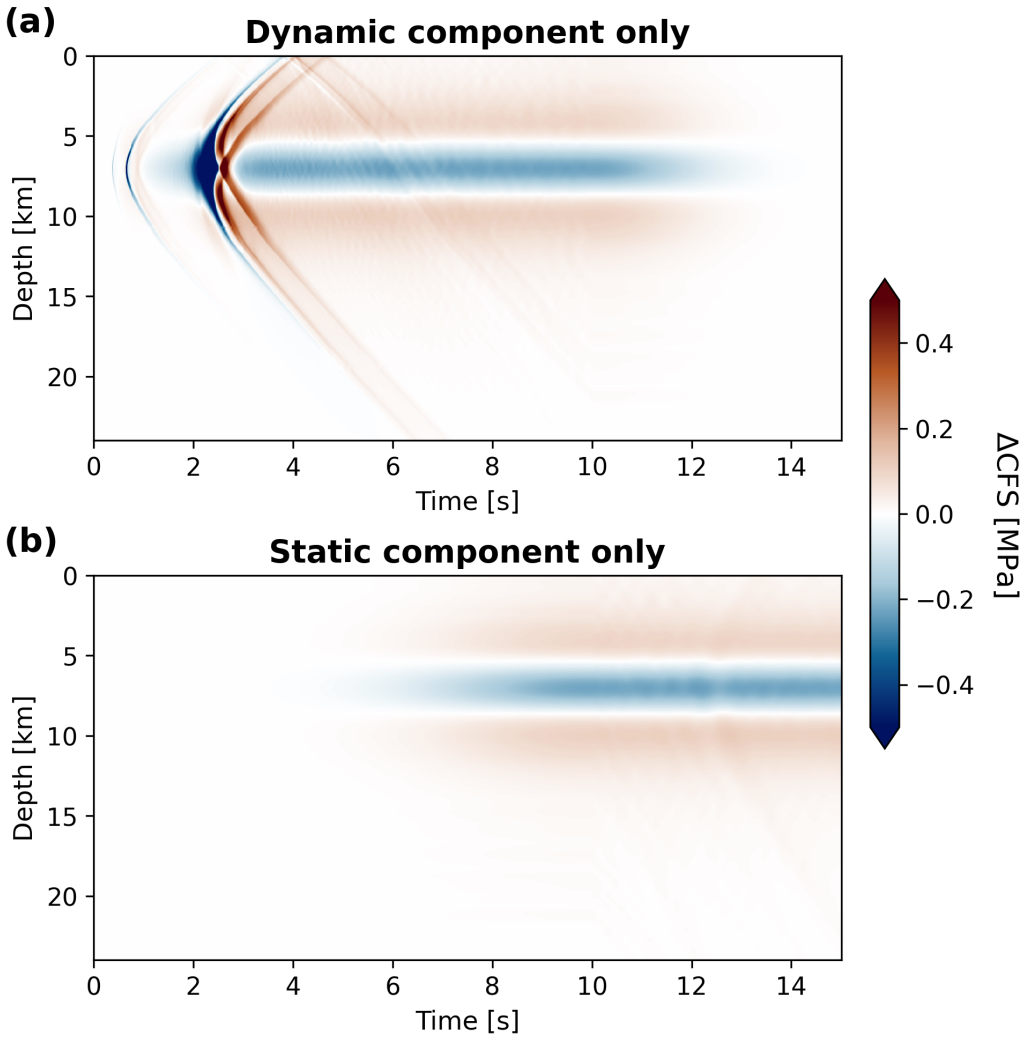

Figure S11. Spatiotemporal evolution of ΔCFS along the mainshock fault in 3D dynamic rupture models for models with (a) only the dynamic component of ΔCFS and (b) only the static component of ΔCFS . Panels (a) and (b) are utilized to generate perturbed SEAS models shown in Figures S12a and S12b, respectively.

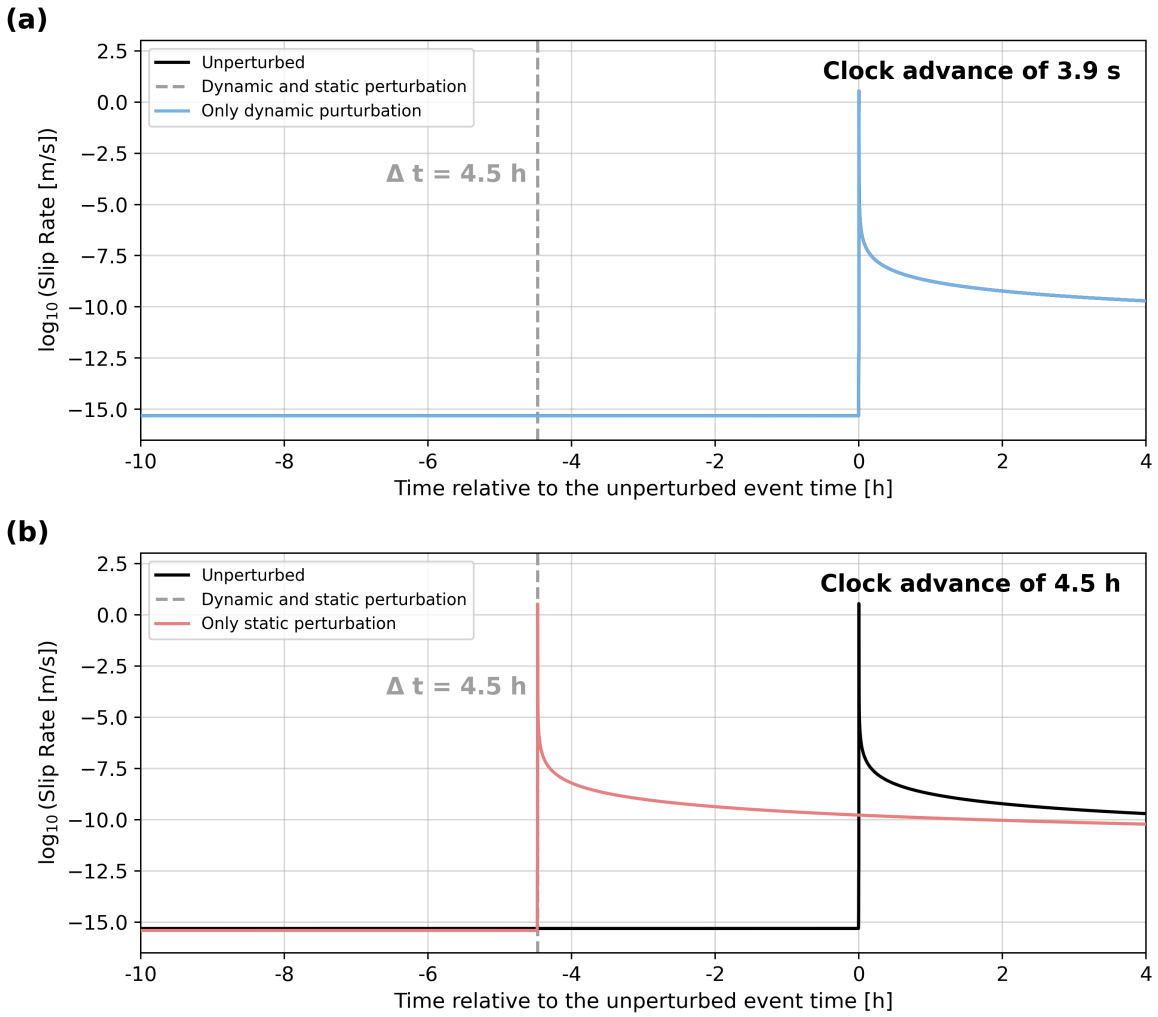

Figure S12. Comparison of the evolution of slip rate when perturbed by both dynamic and static components of ΔCFS (grey) with the slip rate when perturbed by (a) only the dynamic component of ΔCFS (see Fig. S11a) and (b) only the static component of ΔCFS (see Fig. S11b). The black line in both panels shows the slip rate evolution of the unperturbed model. These examples are generated by perturbing target mainshock event 282 in the reference aging law SEAS model (7.82 km; Fig. S3b) using the stress perturbation from the dynamic rupture model with a vertical foreshock fault, slow initiation (VSI), and a 340° strike orientation of the mainshock fault.

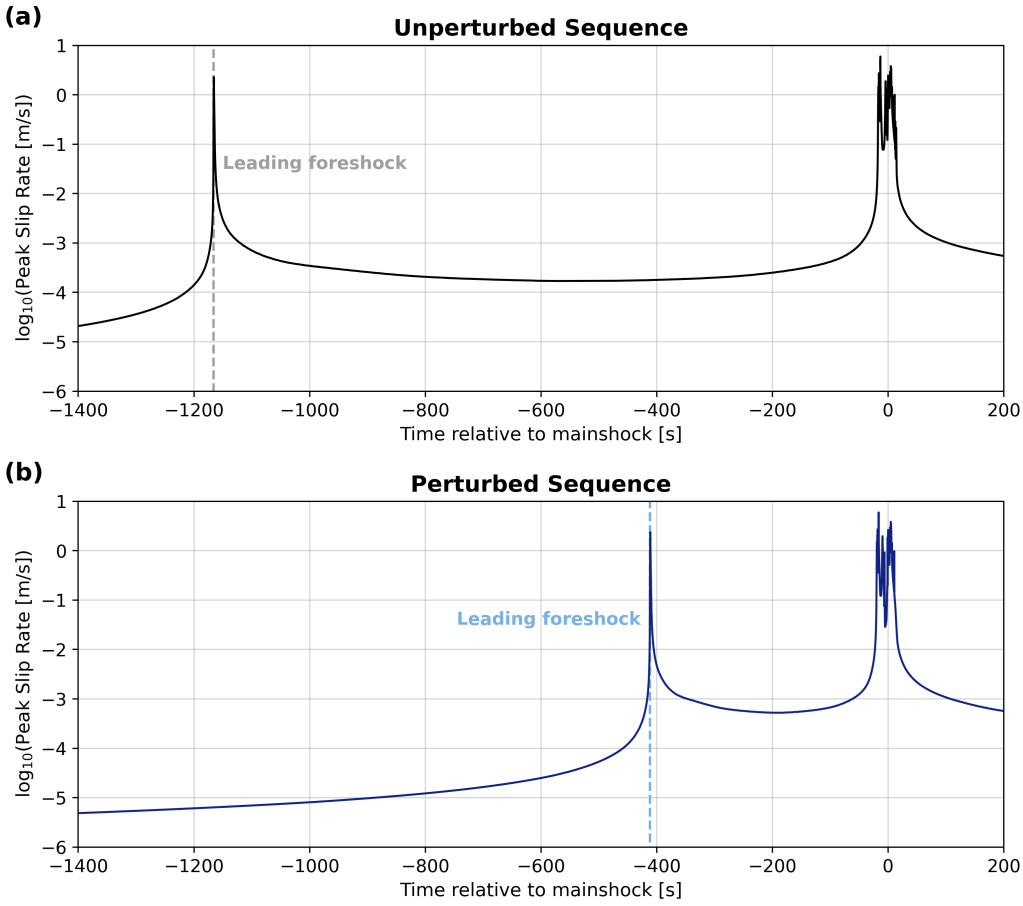

Figure S13. Shortening of the duration of the cascading foreshock-mainshock sequence in the SEAS model. Peak slip rate evolution of (a) the unperturbed model and (b) the perturbed model. The time from the leading foreshock (dashed lines) to the mainshock (zero in x-axis) reduces from 1,166 s in the unperturbed sequence (a) to 411 s in the perturbed sequence (b). This example is generated by perturbing event 120 (at 6.5 km depth) in the reference aging law SEAS model using the stress perturbation from the dynamic rupture model with the vertical foreshock fault, slow initiation (VSI) with 340° strike orientation of the mainshock fault.

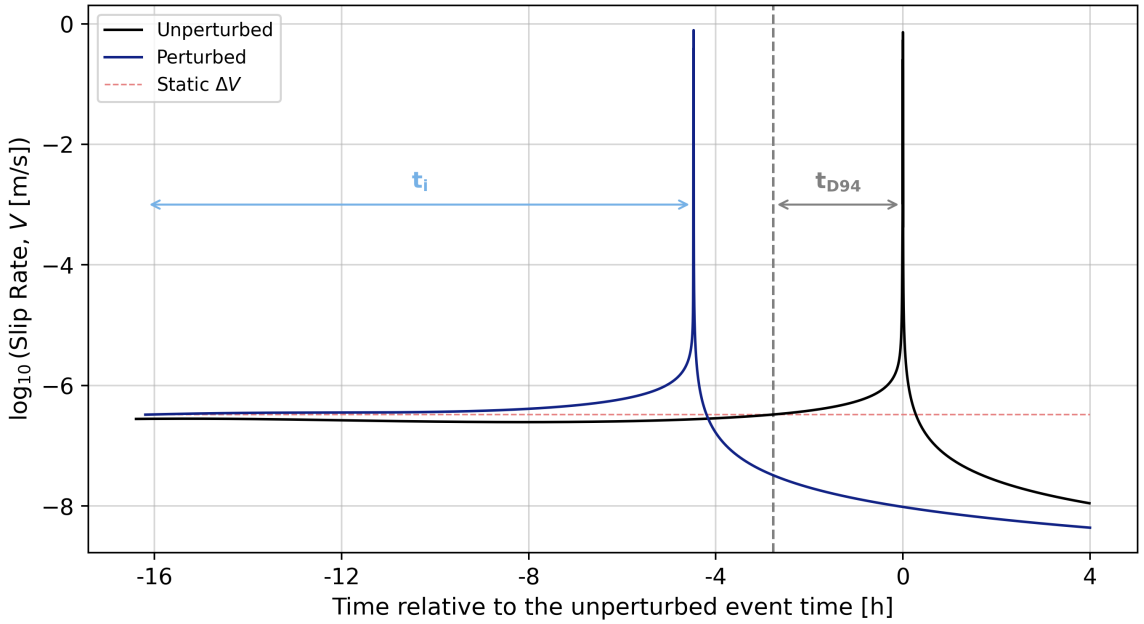

Figure S14. Comparison of time to instability measured from our SEAS simulation (t_i, blue arrow) to that predicted from a 1D spring-slider solution (t_{D94}, grey arrow; Dieterich, 1994). Slip rate evolutions of the unperturbed model (black) and the perturbed model (dark blue) are obtained at a depth corresponding to the maximum aseismic slip during the perturbation period in each simulation (z_{max} = 3.44 km). This depth corresponds to velocity-weakening behavior. The pink dotted line shows the quasi-constant increase in slip rate due to the perturbation and the grey dashed line marks the time when the slip rate in the unperturbed model reaches the increased slip rate. This example is generated by perturbing target mainshock event 282 (at 7.82 km depth; Fig. S3b) using the dynamic stress perturbation from the dynamic rupture model with the vertical foreshock fault, slow initiation (VSI) with 340° strike orientation of the mainshock fault.

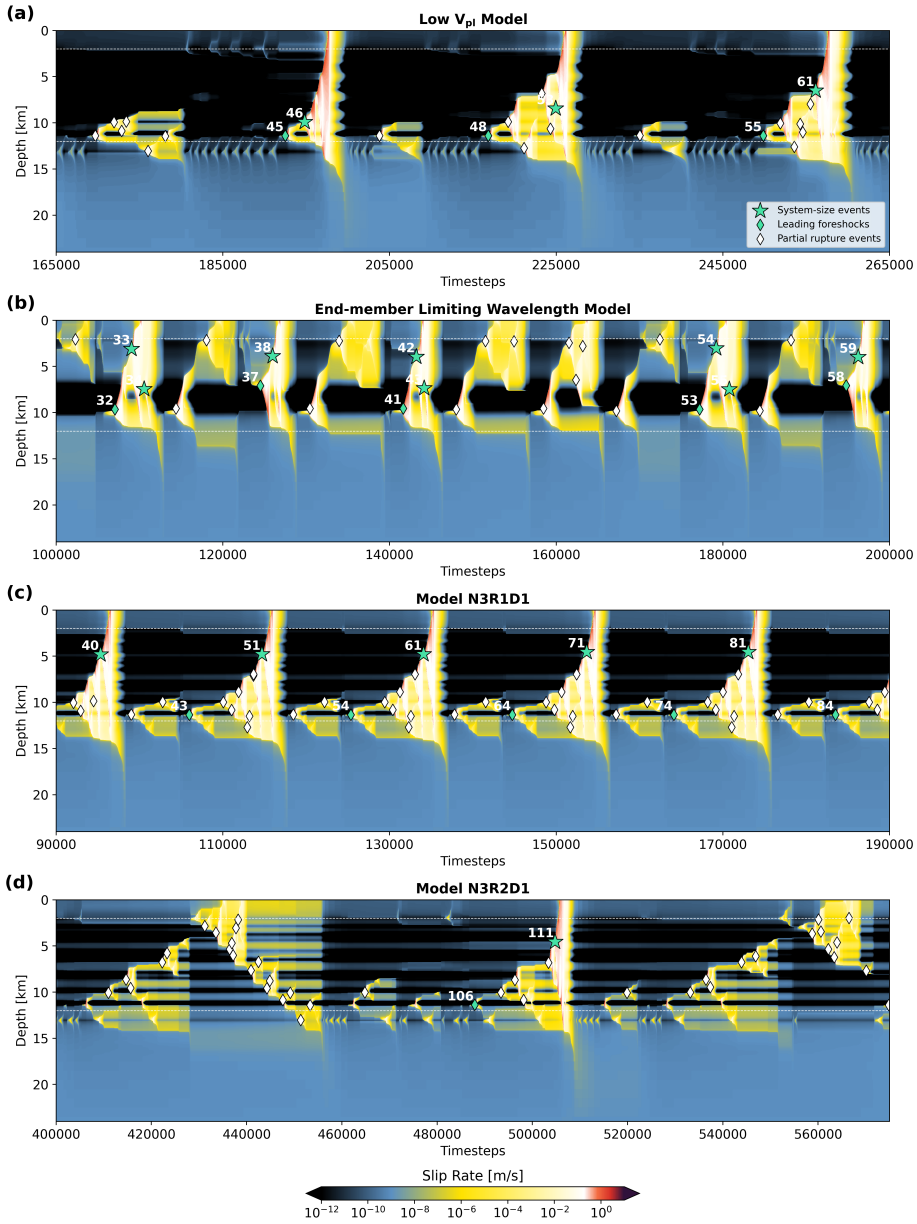

Figure S15. Spatiotemporal evolution of slip rate for the four additional SEAS models. (a) Model with $V_{\mathrm{pl}} = 3.2 \times 10^{-11}$ m/s, showing the period between 11520 yr and 19880 yr of simulation time. (b) Model with fractal heterogeneity in all three parameters (σ_n, $(a-b)$, and D_{RS}) using minimum and maximum wavelengths of 30 m and 10 m, respectively, showing the period between 338 yr and 710 yr of simulation time. (c) Model N3R1D1 in YGMF1, showing the period between 348 yr and 679 yr of simulation time. (d) Model N3R2D1 in YGMF1, showing the period between 387 yr and 537 yr of simulation time.

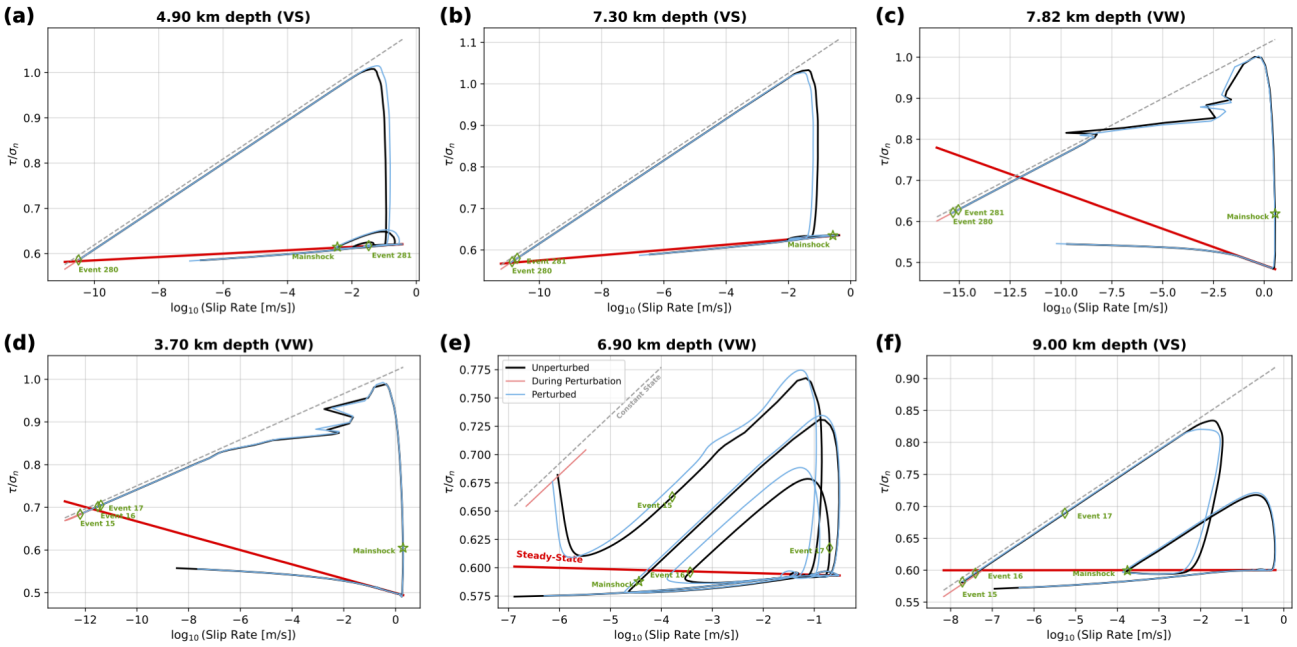

Figure S16. Phase diagram across different depths and in multiple scenarios. (a-c) Phase diagram for the same scenario shown in Figure 9 of the main text, but plotted at (a) 4.9 km (VS patch), (b) 7.3 km (VS patch), and (c) 7.82 km (mainshock hypocenter depth). (d-f) Phase diagram for a clock delay model shown in Figure 8b (model A10; target mainshock event 18), plotted at (d) 3.7 km (mainshock hypocenter depth), (e) 6.9 km (depth of maximum ongoing slip, z_{max}), and (f) 9.0 km (VS patch). VS: velocity-strengthening, VW: velocity-weakening.

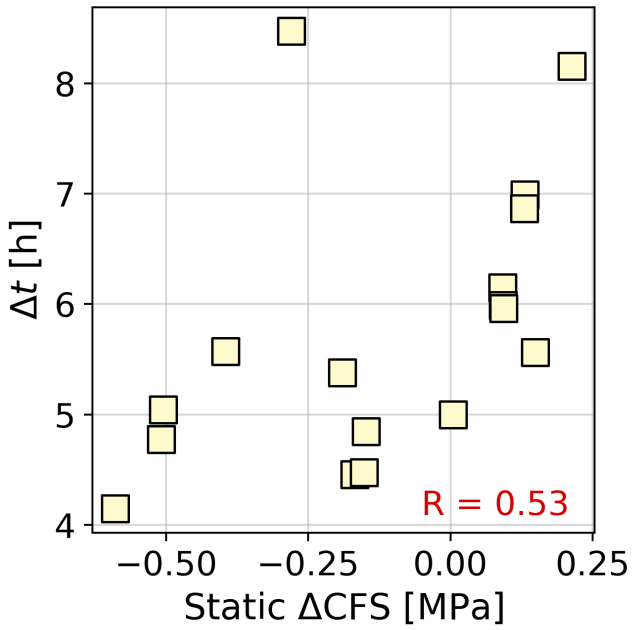

Figure S17. Same as Figure 4b of the main text, but measured at the target hypocenter depth in each unperturbed model. Note negative static ΔCFS values even for mainshock clock advance models (i.e., $\Delta t > 0$).